ORCA – Online Research @ Cardiff

This is an Open Access document downloaded from ORCA, Cardiff University's institutional repository:https://orca.cardiff.ac.uk/id/eprint/161832/

This is the author’s version of a work that was submitted to / accepted for publication.

Citation for final published version:

Ma, Lijun, Du, Lena, Wang, Shu, Wang, Qing, Xue, Shifeng, Zhu, Hanxing and Liu, Qian 2023. Dimension-dependent mechanical features of Au-nanocrystalline nanofilms. Nano Research 16 (12) , pp. 13400-13408. 10.1007/s12274-023-6091-2

Publishers page: https://doi.org/10.1007/s12274-023-6091-2

Please note:
Changes made as a result of publishing processes such as copy-editing, formatting and page numbers may not be reflected in this version. For the definitive version of this publication, please refer to the published source. You are advised to consult the publisher’s version if you wish to cite this paper.

This version is being made available in accordance with publisher policies. See http://orca.cf.ac.uk/policies.html for usage policies. Copyright and moral rights for publications made available in ORCA are retained by the copyright holders.

ISSN 1998-0124 CN 11-5974/O4
https://doi.org/10.1007/s12274-023-6091-2

Dimension-dependent mechanical features of Au-nanocrystalline nanofilms

Lijun Ma[1,2,§], Lena Du[3,§], Shu Wang[2], Qing Wang[6], Shifeng Xue[1](✉), Hanxing Zhu[4](✉), Qian Liu[2,5](✉)
[1] Department of Engineering Mechanics, College of Pipeline and Civil Engineering, China University of Petroleum (East China), Qingdao 266580, China
[2] CAS Center for Excellence in Nanoscience, National Center for Nanoscience and Technology &amp; University of Chinese Academy of Sciences, Beijing 100190, China
[3] Department of Physics, Capital Normal University, Beijing 100048, China
[4] School of Engineering, Cardiff University, Cardiff CF24 3AA, UK
[5] MOE Key Laboratory of Weak-Light Nonlinear Photonics, TEDA Applied Physics Institute, School of Physics, Nankai University, Tianjin 300457, China
[6] College of Mechanical and Architectural Engineering, Taishan University, Tai'an 271000, China
[§] These authors contributed equally

Nano Res., **Just Accepted Manuscript** • https://doi.org/10.1007/s12274-023-6091-2
http://www.thenanoresearch.com on Aug. 16, 2023

Just Accepted

This is a "Just Accepted" manuscript, which has been examined by the peer-review process and has been accepted for publication. A "Just Accepted" manuscript is published online shortly after its acceptance,which is prior to technical editing and formatting and author proofing. Tsinghua University Press (TUP) provides "Just Accepted" as an optional and free service which allows authors to make their results available to the research community as soon as possible after acceptance. After a manuscript has been technically edited and formatted, it will be removed from the "Just Accepted" Web site and published as an ASAP article. Please note that technical editing may introduce minor changes to the manuscript text and/or graphics which may affect the content, and all legal disclaimers that apply to the journal pertain. In no event shall TUP be held responsible for errors or consequences arising from the use of any information contained in these "Just Accepted" manuscripts. To cite this anuscript please use its Digital Object Identifier (DOI®),which is identical for all formats of publication.

Address correspondence to First A. Firstauthor, email1; Third C. Thirdauthor, email2

TABLE OF CONTENTS (TOC)

Dimension-dependent mechanical features of Au-nanocrystalline nanofilms

Lijun Ma[1,2], Lena Du[3], Shu Wang[2], Qing Wang[6], Shifeng Xue[1,*], Hanxing Zhu[4,*], and Qian Liu[2,5,*]

[1] Department of Engineering Mechanics, College of Pipeline and Civil Engineering, China University of Petroleum (East China), Qingdao 266580, China

[2] CAS Center for Excellence in Nanoscience, National Center for Nanoscience and Technology & University of Chinese Academy of Sciences, Beijing 100190, China

[3] Department of Physics, Capital Normal University, Beijing 100048, China

[4] School of Engineering, Cardiff University, Cardiff CF24 3AA, UK

[5] MOE Key Laboratory of Weak-Light Nonlinear Photonics, TEDA Applied Physics Institute, School of Physics, Nankai University, Tianjin 300457, China

[6] College of Mechanical and Architectural Engineering, Taishan University, Tai'an 271000, China

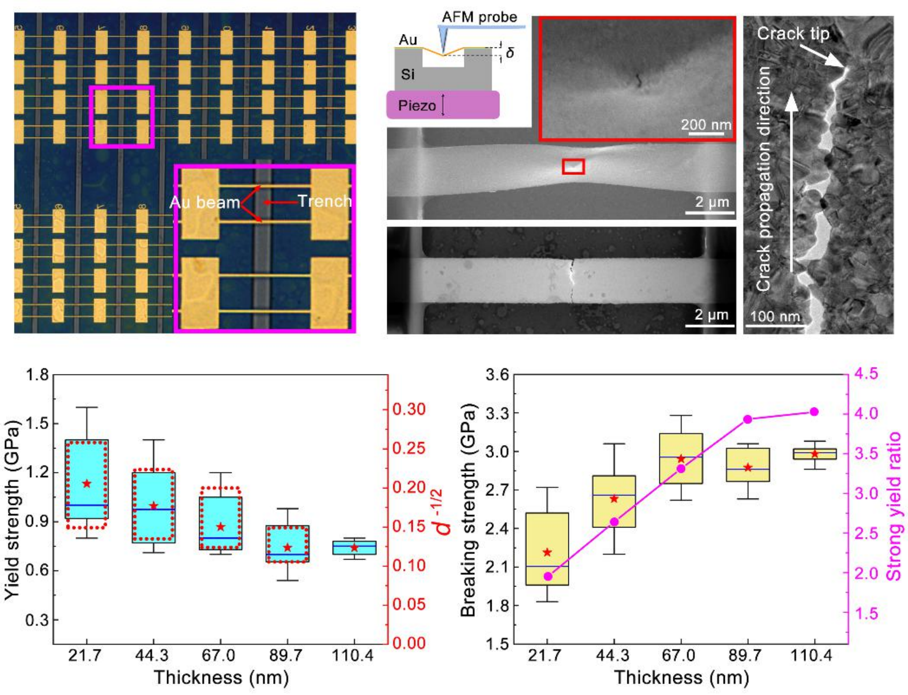

Study on mechanical properties with statistical significance of gold nanofilms demonstrate a strong dimension-dependent nonlinear feature and the strong-yield ratio as well as a still valid Hall-Petch relationship at the nanoscale.

Nano Research

ISSN 1998-0124 CN 11-5974/04
https://doi.org/(automatically inserted by the publisher)

Research Article

Dimension-dependent mechanical features of Au-nanocrystalline nanofilms

Lijun Ma[1,2,§], Lena Du[3,§], Shu Wang[2], Qing Wang[6], Shifeng Xue[1](✉), Hanxing Zhu[4](✉), and Qian Liu[2,5](✉)

[1] *Department of Engineering Mechanics, College of Pipeline and Civil Engineering, China University of Petroleum (East China), Qingdao 266580, China*
[2] *CAS Center for Excellence in Nanoscience, National Center for Nanoscience and Technology & University of Chinese Academy of Sciences, Beijing 100190, China*
[3] *Department of Physics, Capital Normal University, Beijing 100048, China*
[4] *School of Engineering, Cardiff University, Cardiff CF24 3AA, UK*
[5] *MOE Key Laboratory of Weak-Light Nonlinear Photonics, TEDA Applied Physics Institute, School of Physics, Nankai University, Tianjin 300457, China*
[6] *College of Mechanical and Architectural Engineering, Taishan University, Tai'an 271000, China*
§ *These authors contributed equally*

© Tsinghua University Press and Springer-Verlag GmbH Germany, part of Springer Nature 2018

Received: day month year / **Revised:** day month year / **Accepted:** day month year (automatically inserted by the publisher)

ABSTRACT

For metal nanofilms composed of nanocrystals, the multiple deformation mechanisms will coexist and bring unique and complex elastic-plastic and fracture mechanical properties. By successfully fabricating large quantities of uniform doubly-clamped suspended gold (Au) nanobeams with different thicknesses and nanograin sizes, we obtain full-spectrum mechanical features with statistical significance by combining AFM nanoindentation experiments, nonlinear theoretical model, and numerical simulations. The yield and breaking strengths of the Au nanobeams have a huge increase by nearly an order of magnitude compared to bulk Au and exhibit strong nonlinear effects, and the corresponding strong-yield ratio is up to 4, demonstrating extremely high strength reserve and vibration resistance. The strong-yield ratio gradually decreases with decreasing thickness, identifying a conversion of the failure type from ductile to brittle. Interestingly, the Hall-Petch relationship has been identified to be still valid at the nanoscale, and *K* in the formula reaches 4.8 GPa·nm$^{1/2}$ nearly twice of bulk nanocrystalline Au, this is ascribed to the coupling effect of nanocrystals and nanoscale thickness.

KEYWORDS

nanocrystalline Au nanobeams, atomic force microscopy, numerical simulations, full-spectrum mechanical properties

1 Introduction

Due to grain boundary constraints on dislocation motion, yield strength of bulk polycrystalline metals increases with decreasing grain size which can be described by the Hall-Petch formula [1, 2]. But when grain size decreases to the nanoscale, grain boundary volume fraction of the bulk polycrystalline metal materials will become quite large, and its deformation mechanism will change from a single dislocation mechanism to the coexistence of multiple deformation mechanisms, resulting in a huge difference of the nanocrystalline metal materials from non-nanocrystalline metal materials in the mechanical properties [3-6].In addition, the grain distribution-induced features are different in the interior and surface of the bulk metal materials, but the difference can be negligible due to little influence on macroscopic mechanical properties. However, for nanocrystalline metals with nanoscale geometric sizes, the surface effect becomes significant, and its mechanical properties are not only affected by grain size but also by grain arrangement that is restricted by geometric shape and size, resulting in different mechanical properties and deformation mechanisms [7, 8]. As a result, nanoparticles [9, 10], nanowires [11-17], and nanofilms [18] have significant differences in mechanical properties due to their different geometric dimensional constraints, resulting in that mechanical properties of the nanoscale nanocrystalline metal materials no longer have a unified description like macroscopic bulk materials.

With the widespread use of nanocrystalline metal nanofilms in semiconductor integrated circuits [19, 20], flexible wearable electronic devices [21-25], nanoelectromechanical systems [26], and so forth, their elastic-plastic and fracture features have become particularly important, which will largely determine the service life and vibration resistance of metal nanofilms [27-29]. So, it is very necessary to accurately obtain the full-spectrum mechanical properties of nanocrystalline metal nanofilms with statistical significance. Nanocrystalline metal nanofilms have an ultra-high surface to volume ratio and grain boundary volume fraction, and the coupling of multiple deformation mechanisms caused by the size and arrangement of nanocrystals and the nanoscale geometrical limitations will make their mechanical properties more diverse. Compared with metal nanowires that have been extensively studied [11-17], the deformation and slip of

---

Address correspondence to Qian Liu, liuq@nanoctr.cn; Hanxing Zhu, zhuh3@cardiff.ac.uk; Shifeng Xue, sfeng@upc.edu.cn

nanocrystals in metal nanofilms are more restricted by the presence of other grains in the in-plane, which makes the deformation and torsion of the grains more difficult than that in nanowires, thereby affecting their elastic-plastic features. Due to the limitation of nanofilm thickness, the size of nanocrystals is often an order of magnitude with thickness, and the arrangement of nanocrystals in the thickness direction is more sensitive to the size of the thickness. It should also be stressed that the preparation method of nanofilms can greatly affect the nucleation, growth, and distribution of grains in the thickness direction [30, 31], thus impacting fracture evolution and ultimate strength of the nanofilms. These factors that must be considered make the full-spectrum mechanical properties of nanocrystalline metal nanofilms more complicated and lead to the obvious dependence of elastic-plastic and fracture response on the size and arrangement of nanocrystals induced by nanoscale geometric dimension. In another hand, the fabrication of uniform suspended nanofilm beams, which can effectively avoid the influence of underlayer and thus can obtain a more realistic intrinsic nature, has been a difficult problem, resulting in no way to realize meaningful test of mechanical properties of metal nanofilms. Owing to the shortage of considering nanograin arrangement and difficulty in the fabrication of suspended metal nanofilms, so far, there are few studies with statistical significance on the elastic-plastic and fracture mechanics properties of nanocrystalline metal nanofilms, making evaluation and use of the metal nanofilms missing scientific foundation.

Here taking nanocrystalline Au nanofilm prepared by the magnetron sputtering deposition as an example, we successfully fabricated large quantities of uniform doubly-clamped suspended nanobeams with different thicknesses and grain sizes using a novel micro/nano fabrication route. Based on the suspended Au nanofilm beams with different nanoscale thicknesses (21~110 nm), the full-spectrum nanomechanical properties of Au nanobeams were systematically studied, and the elastic and plastic force-displacement (*F*-*δ*) curves with statistical significance, for the first time, were obtained by nanoindentation method of atomic force microscope (AFM) with high force-sensing capabilities and spatial resolution [11-14, 32-34]. Considering the strong geometric nonlinearity and material nonlinearity exhibited by the suspended Au nanobeam under large displacement, the nonlinear elastic continuum theory and finite element method (FEM) were used to fit the *F*-*δ* curves for determining the elastic modulus, prestress, yield and breaking strengths, and strong-yield ratio. Mechanical enhancement effects induced by the coupling of nanocrystals with different sizes, arrangements and thicknesses were analyzed by examining the morphological characteristics of nanograins, crack initiation, propagation, and failure process of the Au nanobeams. Interestingly, the Hall-Petch formula is still valid at the nanoscale and has a significant enhancement in *K* value relating to grain boundary.

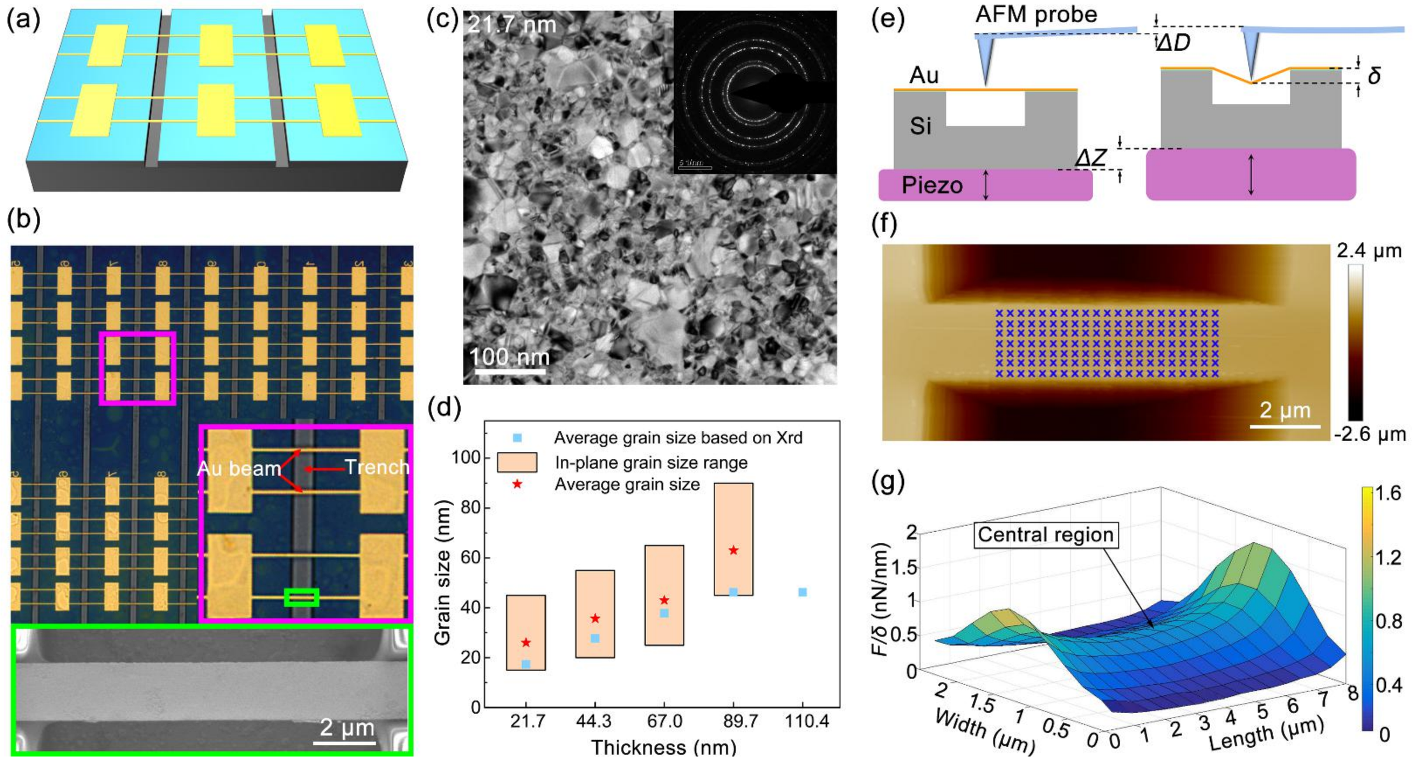

Figure 1 Doubly-clamped suspended Au nanobeams and nanoindentation measurement based on the QNM of AFM. (a) Schematic diagram of the Au nanobeam array. (b) The upper panel shows the optical microscopy image of the Au nanobeam array, and the lower panel shows the SEM (scanning electron microscopy) image of a suspended Au nanobeam. (c) TEM image of the 21.7 nm thick Au beam. (d) The statistical diagram of the grain size distributions of Au nanofilms with different thicknesses. (e) Schematic diagram of the AFM nanoindentation suspended Au beam. (f) The AFM characterization of the suspended Au beam before nanoindentation. The crosses on the surface of the suspended Au beam represent the schematic diagram of the elastic nanoindentation loading point array based on the QNM. (g)

2 Experimental

The large-scale arrays of suspended doubly-clamped Au beams with 5 different thicknesses (21.7 nm, 44.3 nm, 67.0 nm, 89.7 nm, and 110.4 nm) were designed and fabricated successfully (Figs. 1(a) and 1(b)) by a series of micro/nano processing procedures (see the Method section and Fig. S1 in the Electronic Supplementary Material (ESM)). Here the suspended Au beams for the same thickness are uniform to ensure test consistence for obtaining data with statistical significance. The transmission electron microscopy

Three-dimensional F/δ distribution diagram of the local suspended region of Au beam based on the QNM.

(TEM) images and X-ray diffraction (XRD) patterns of the suspended Au beams with different thicknesses are shown in Figs. 1(c) and S2. The grain size distributions were obtained (Fig. 1(d)) through both XRD results calculated by the Scherrer formula [35] (the Method section) and the statistic measurement of the TEM result, showing that the average grain size gradually decreases with a decrease in film thickness. The schematic diagram of the AFM nanoindentation for the suspended Au nanobeam is shown in Fig. 1(e). The Peak Force Quantitative Nano-Mechanical method (QNM) of AFM was adopted to perform a mapping indentation with a constant loading to the suspended area to obtain F-δ curves at all points and determine the midpoint of the sample. The AFM morphology characterization of the Au nanobeam (Fig. 1(f)) adopted the tipping mode, where the blue “X” array in the suspended Au nanobeam represents the nanoindentation points of the mapping. The F/δ distribution map presents a three-dimensional saddle shape (Fig. 1(g)). The exact midpoint of the suspended Au nanobeam is located at the lowest F/δ in length and the highest position in width, and the corresponding F-δ curve can be obtained by indentation test of the midpoint using AFM. More details on AFM probes selection, calibration, and nanoindentation measurements are presented in the Method section.

3 Results and discussion

3.1 Elasticity

Elastic modulus can be accurately calculated from the F-δ response to the elastic deformation of nanoscale nanocrystalline Au beams. The F-δ curves at the midpoint of four loading cycles were obtained (Fig. 2(a)) under step-by-step cyclic loading for a 21.7 nm thick Au beam. The high coincidence of the F-δ curves under different loads well indicates the stability of the doubly-clamped Au nanobeam and measurement repeatability. The doubly-clamped Au nanobeams with different thicknesses were measured to obtain sufficient F-δ data for valid statistics. A nonlinear elastic continuum mechanics model [36, 37] based on the variational method was introduced to consider the initial stress effect and describe the nonlinear F-δ relationship of doubly-clamped Au nanobeams under the nanoindentation.

$$F = 16Ew\left(\frac{t}{l}\right)^3\delta + \sigma_0 t\delta + \frac{8}{3}Ewt\left(\frac{\delta}{l}\right)^3 \quad (1)$$

Where F and δ are the applied force and displacement at the midpoint of the nanobeam, respectively. E is the elastic modulus, σ_0 is the prestress, and w, t, and l refer to the width, thickness, and length of the nanobeam, respectively. The three terms in Eq. (1) represent in turn the linear elastic bending contribution, the prestress contribution, and the tensile contribution caused by the large deformation. The contributions of these three terms to the total load vary with indentation displacement and the thickness are shown in Section S2 and Fig. S3 in the ESM. This theoretical model takes into account the stiffness enhancement caused by the prestress and additional tension. The increased stiffness induced by prestress mainly influences the F-δ response of thinner Au nanobeams under smaller displacement indentation, while the increased stiffness induced by tension dominates the F-δ response under larger

Figure 2 F-δ curves and fitting results of elastic modulus and prestress. (a) The F-δ curves under four step-by-step nanoindentation and curves fitting to Eq. (1) for a 21.7 nm thick Au beam. (b and c) The histogram of elastic modulus and prestress for 21.7 nm thick Au beam, the blue dot-dash lines represent the fitted Gaussian distribution. (d) The box-plots of elastic modulus for Au nanobeams with different thicknesses. (e) MD model with an average grain size of 15 nm and thickness of 40 nm. (f) the elastic modulus and Poisson's ratio of Au nanofilms with different grain sizes and thicknesses based on MD simulations. Each plot includes the minimum, lower quintile, median (horizontal line), mean (magenta star), upper quintile, and maximum in (d).

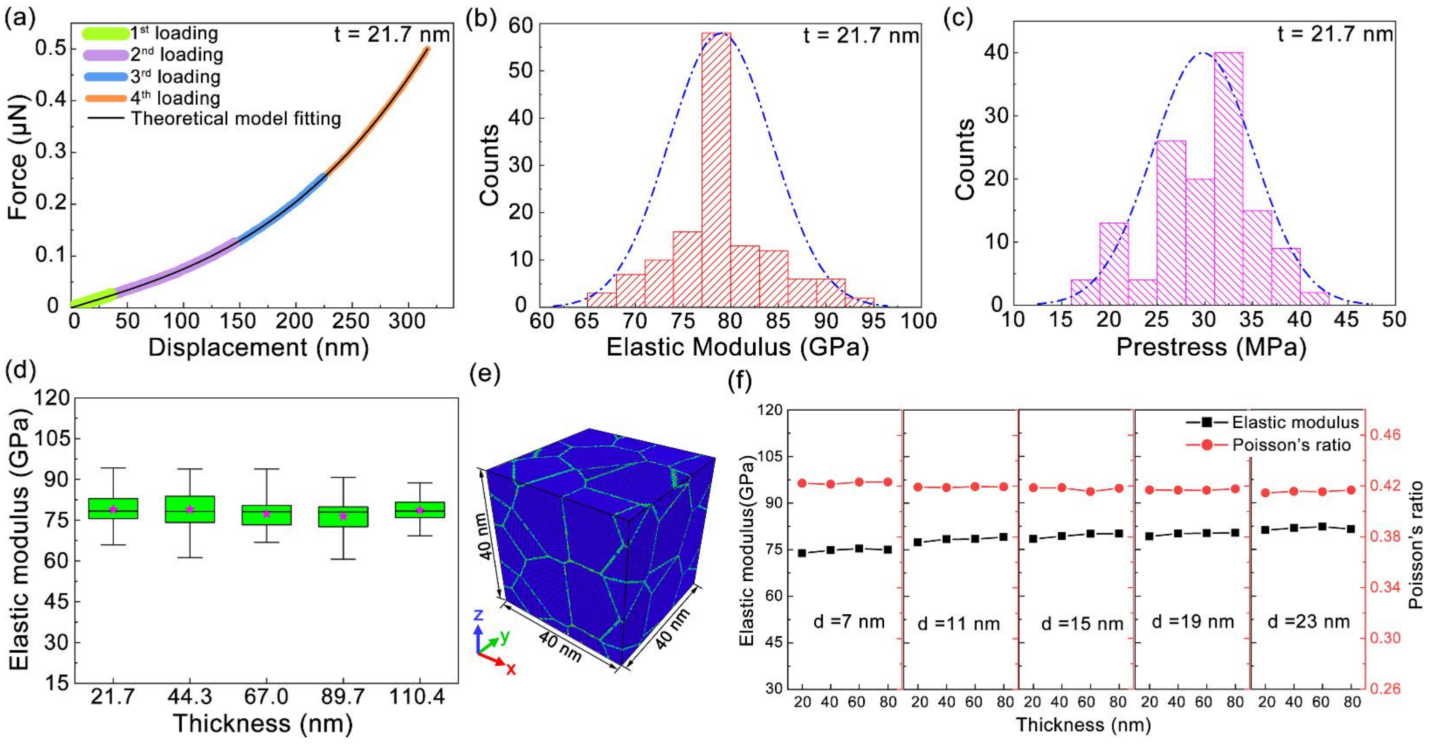

ISSN 1998-0124 CN 11-5974/04
https://doi.org/(automatically inserted by the publisher)

displacement indentation, and the load-bearing mechanism of the beam gradually changes from the bending-dominated mode to the stretching-dominated mode with the increase of indentation displacement, showing a typical geometric nonlinear elastic effect under large elastic deformation.

Combined with the geometric dimensions of each Au nanobeam, the *F*-*δ* curves of the Au nanobeams with different thicknesses can be fitted by the least square method using Eq. (1), and the corresponding elastic modulus and prestress can be calculated. In Fig. 2(a), the fitting results of Eq. (1) and the experimental *F*-*δ* curve of a 21.7 nm thick Au beam highly coincided, confirming the credibility of the theoretical model describing the elastic deformation behavior of the Au nanobeams under nanoindentation. The histograms of elastic modulus and prestress for the 21.7 nm thick Au beam shows good statistical distribution of data, which are supported by fitted blue dot-dash Gaussian distribution curves (Figs. 2(b) and 2(c)). The distribution of elastic modulus concentrates upon about 78 GPa, and the distribution of the prestress mainly concentrates upon the range of 20~40 MPa. And *F*-*δ* curves of other thicknesses Au nanobeams were also fitted for obtaining the statistical results of elastic modulus and prestress (Section S3 and Fig. S4). The elastic modulus of the Au nanobeams with 5 different thicknesses (Fig. 2(d)) is near 78 GPa very close to bulk Au, indicating that elastic modulus is not noticeably affected by the geometric dimensions and grain size. This result is also confirmed by using molecular dynamics (MD) simulation (Figs. 2(e) and 2(f); Section S4 in the ESM). While the distribution of prestress is slightly scattered (Figs S4(e)-S4(h) in the ESM) due to being randomly introduced during the processing and transferring of the Au nanobeams. The rationality of such prestress distribution can be proven based on the buckling theory of beams (Section S5 and Fig. S5 in the ESM).

3.2 Yield and breaking

Fracture failure experiments of the Au nanobeams were implemented (the Method section) by using a 21.7 nm thick Au beam, the parabolic *F*-*δ* curve (Fig. 3(a)) exhibits a strong nonlinear effect under large displacement indentation, indicating an enhancement of Au nanobeam in stiffness with an increase in indentation displacement. It should be noted that force can suddenly drop to zero when the Au nanobeam is completely broken. Furthermore, all *F*-*δ* curves of fracture failure for Au nanobeams with different thicknesses are akin, as shown in Fig. 3(a). For all *F*-*δ* curves, breaking loads as a function of the thickness are presented in Fig. 3(b), showing an approximately linear increase with an increase in nanoscale thickness. Meanwhile, AFM images reveal that the Au nanofilm has undergone a significant plastic deformation before it is completely broken (Fig. S6 in the ESM), which is very easy to ignore, but also more important. In the plastic deformation stage, doubly-clamped Au nanofilms exhibit strong material nonlinearity, geometric nonlinearity, and contact nonlinearity. Especially, considering the influences of the prestress, the geometric sizes, and the large stress gradient at the nanoindentation position, it

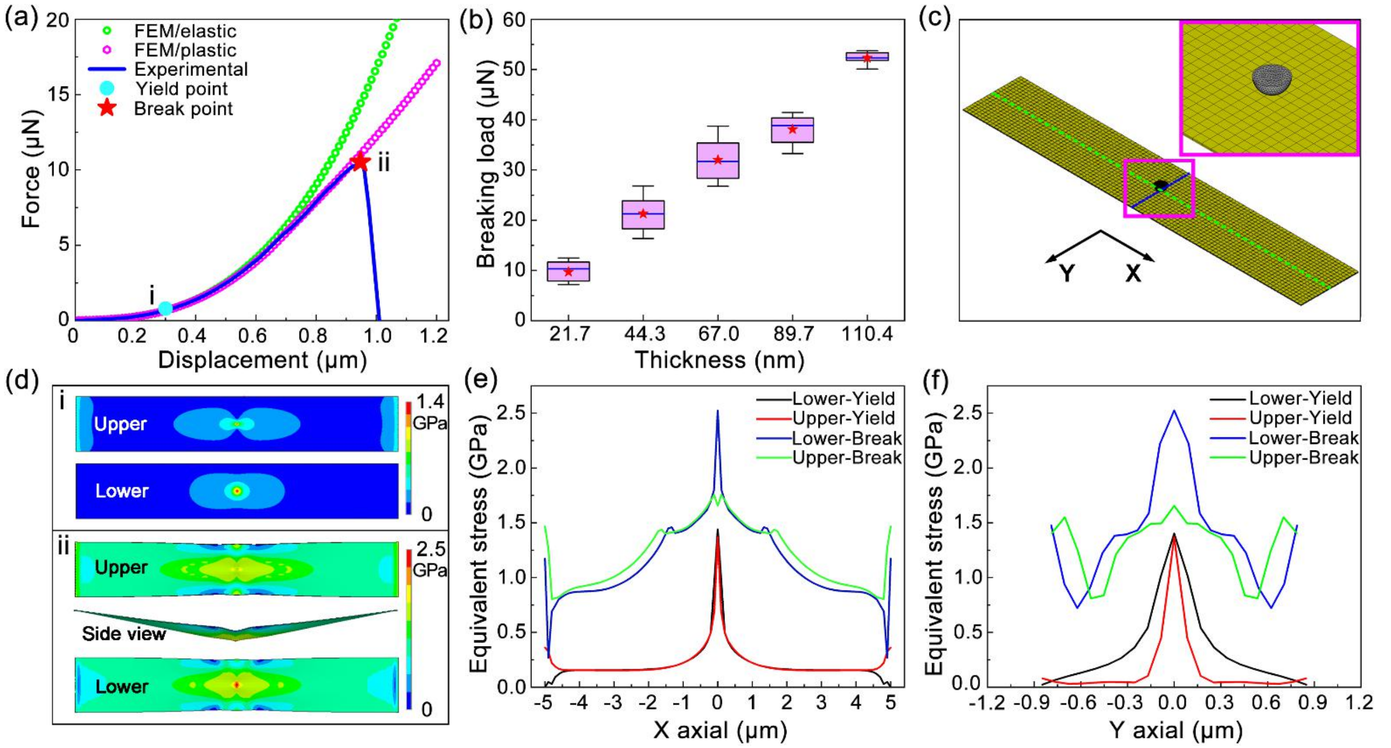

Figure 3 The *F*-*δ* curves of fracture failure and FEM results of a 21.7 nm thick Au beam under nanoindentation. (a) The experimental *F*-*δ* curve and fitting using FEM. (b) Breaking load as a function of the thickness. (c) Finite element model and meshing. (d) Equivalent stress distributions in both the upper and lower surfaces of the Au beam at (i) yield point and (ii) break point. (e and f) Equivalent stress distributions along (e) the green dash line (X-axis direction) and (f) the blue dash line

(Y-axis direction) of the beam shown in (c) when it begins to yield or fracture. Each plot includes the minimum, lower quintile, median (horizontal line), mean (red star), upper quintile, and maximum in (b).

is very difficult to establish an elastic-plastic theoretical model describing the relationship between the force and displacement for an analytical solution. Therefore, numerical simulation using FEM with great advantages becomes an alternative means to solve the problem [38-40].

Taking the fracture experiment of a 21.7nm-thick Au beam (Fig. 3(a)) as an example, the corresponding three-dimensional finite element model (Fig. 3(c)) is established (Section S6 and Fig. S7 in the ESM). To calculate the yield strength of nanoscale nanocrystalline Au beams, an inverse approach was used. Different yield strength values were set in the FEM, and the *F*-*δ* curves corresponding to each yield strength obtained from FEM were compared with the experimentally measured curve to match the actual yield strength of the experimental sample. The experimental *F*-*δ* curve of fracture failure and the fitted curves by FEM analyses based on the linear elastic constitutive model (elastic model) and the bilinear isotropic hardening elastoplastic constitutive model (plastic model) with a yield strength of 1.4 GPa are shown in Fig. 3(a). When the indentation loading in the elastic deformation stage is below the yield point of the Au nanofilm, the FEM results obtained from the elastic and plastic models can well fit our experimental results, further identifying the correctness of FEM analyses. When the applied load reaches the yield point (1.4 GPa), plastic deformation starts to occur at the nanoindentation position. The *F*-*δ* curve obtained from FEM based on the elastic model gradually deviates from the experimental curve, and the *F*-*δ* curve obtained from FEM based on the plastic model still maintains a high fitting degree with the experimental curve until the Au nanobeam fractures, showing that the plastic model can accurately describe the elastic-plastic deformation of the Au nanobeam under plastic limit nanoindentation. A longer range of elastoplastic transition and plastic deformation stages resulting from complex microstructure and various deformation mechanisms exhibits a very large load carrying capacity for nanocrystalline Au nanofilms. The equivalent stress distributions obtained by FEM in both the upper and lower surfaces of the 21.7 nm-thick Au nanobeam at the yield and break points under nanoindentation are shown in Fig. 3(d). When yield occurs, the stress obviously concentrates upon the upper and lower surfaces at the probe tip contact area of the Au nanobeam. When the plastic limit failure occurs, the maximum equivalent stress occurs at the middle region of the lower surface. At the yield point and break point, the equivalent stress distributions in both the upper and lower surfaces along the X-axis and Y-axis corresponding to green and blue dash lines shown in Fig. 3(c) have an obvious difference, as illustrated in Figs. 3(e) and 3(f) respectively, showing a dependence on nanobeam shape.

Further research indicates that all *F*-*δ* curves of fracture failure can well be fitted by the FEM results obtained from the plastic model to determine the yield strength (Fig. 4(a)). With an increase in Au nanobeam thickness from 21.7 nm to 110.4 nm, the average yield strength decreases gradually from 1.13 GPa to 0.74 GPa, indicating a very strong thickness dependence and nonlinear enhancement compared to submicron-thick (0.3-1μm) polycrystalline Au films (55-200 MPa) [41]. Based on the fitted *F*-*δ* curves and the breaking loads, the breaking strength of the Au nanobeams can be obtained from the FEM results. With an increase in nanocrystalline Au-film thickness, the breaking strength first increases and then stabilizes at about 3 GPa (Fig. 4(b)). Thinner Au nanobeams composed of smaller nanograins have a relatively higher yield strength and lower breaking strength. The decreasing nanograin size with thickness tends to restrict deformation within grains, increasing yield strength and reducing its contribution to effective plastic deformation. Thus, defects like holes are easily generated under nanoindentation, eventually inducing a decrease in breaking strength. In order to evaluate the comprehensive mechanical properties required by nanocrystalline Au nanofilms in various application scenarios, one concept of strong-yield ratio (measured breaking strength divided by measured yield strength) is introduced (Fig. 4(b)). As the thickness increases, the strong-yield ratio increases from 2 to 4, *i.e.*, the larger the thickness, the better the vibration resistance and strength reserve.

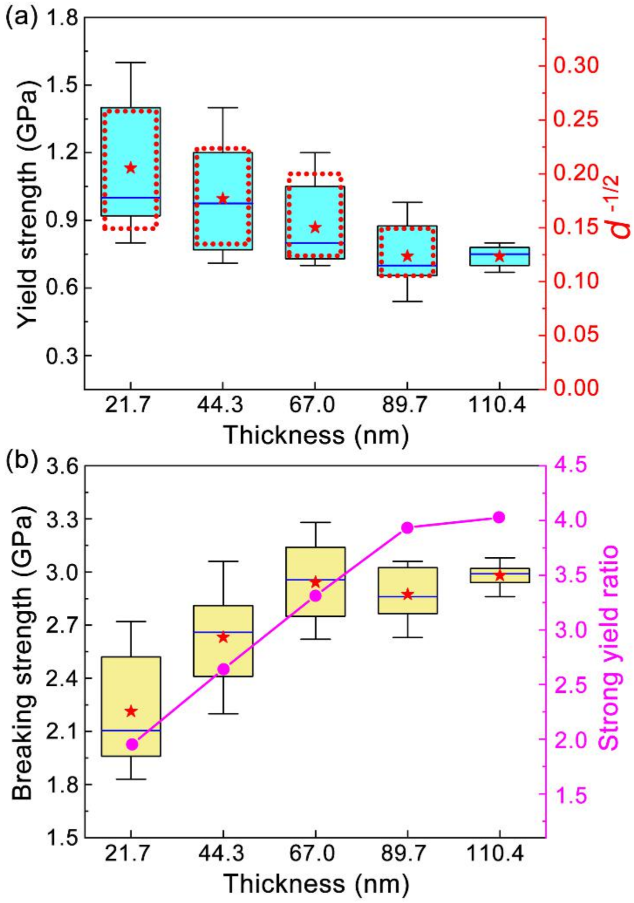

Figure 4 Statistical results of the yield strength and breaking strength as a function of Au beam thickness. (a) The box-plots of yield strength and $d^{-1/2}$. (b) The box-plots of breaking strength and strong-yield ratio. Each plot includes the minimum, lower quintile, median (horizontal line), mean (red star), upper quintile, and maximum.

The initial plastic deformation resistance of polycrystals is largely affected by grain boundaries, which are directly related to grain size. The relationship between the yield strength σ_s and the grain size d of submicron and above for polycrystalline bulk metallic materials can be expressed by the well-known Hall-Petch formula [1, 2]:

$$\sigma_s = \sigma_0 + Kd^{-1/2} \qquad (2)$$

Where σ_0 reflects the resistance to deformation within the crystal, which is equivalent to the yield strength of a very large single crystal. K is usually a constant for a polycrystalline material at room temperature, considered as an influence coefficient relating to grain boundary structure. However, due to the influence of many factors, there are still many difficulties and controversies in experimental verification and physical mechanism for the applicability of the Hall-Petch formula to nanocrystalline metal nanofilms with a very large surface to volume ratio [42]. By an approximate linear fitting (the red-dotted rectangle in Fig. 4(a)) for nanocrystalline Au nanobeams through TEM characterization, the Hall-Petch formula is proven to be still valid in the nanoscale. However, in this case, the calculated K is around 4.8 GPa·nm$^{1/2}$ (σ_0 = 0.15 GPa), showing an abnormal increase compared to 2.5 GPa·nm$^{1/2}$ of the bulk nanocrystalline Au [43], which might mainly originate from the strengthening brought by nanoscale geometric dimensions. In addition, extensive MD simulations reveal that until the grain size down to a region of 30~10 nm, an inverse Hall-Petch effect will occur and reduce the yield strength [44, 45]. The change is due to the transition of deformation mechanism from dislocation-dominated strain hardening to grain rotation and slippage-dominated softening. Experimentally, there are still some controversies about the critical grain size of a polycrystalline metallic material that causes a shift in performance. Our results indicate that Au nanofilms in such a nanograin size range do not exhibit an inverse Hall-Petch effect. Meanwhile, MD simulation results of the Au nanobeam with an average grain size of 10 nm under nanoindentation exhibit multiple deformation mechanisms involving dislocation nucleation from grain boundary, dislocation motion and pile-up, grain boundary migration, and grain rotation (Section S7 and Fig. S8 in the ESM). These mechanisms either cooperate or compete with one another, leading to complicated mechanical properties which decide tolerable levels of stress and stability of microstructure.

3.3 Fracture evolution

Owing to the importance of nanocrystalline-induced fracture evolution and failure mechanism of Au nanofilms under plastic limit nanoindentation, they need to be deeply analyzed. As shown in Fig. 5(a), an obvious plastic deformation occurs at the middle area of Au nanobeam for a large nanoindentation displacement, and the inset of Fig. 5(a) suggests that the initial crack is introduced by the probe tip at the indentation position of the beam. Generally, the crack originates from the position applied the largest stress, and first occurs on the lower surface of the nanobeam (Fig. 3(d)). Under the

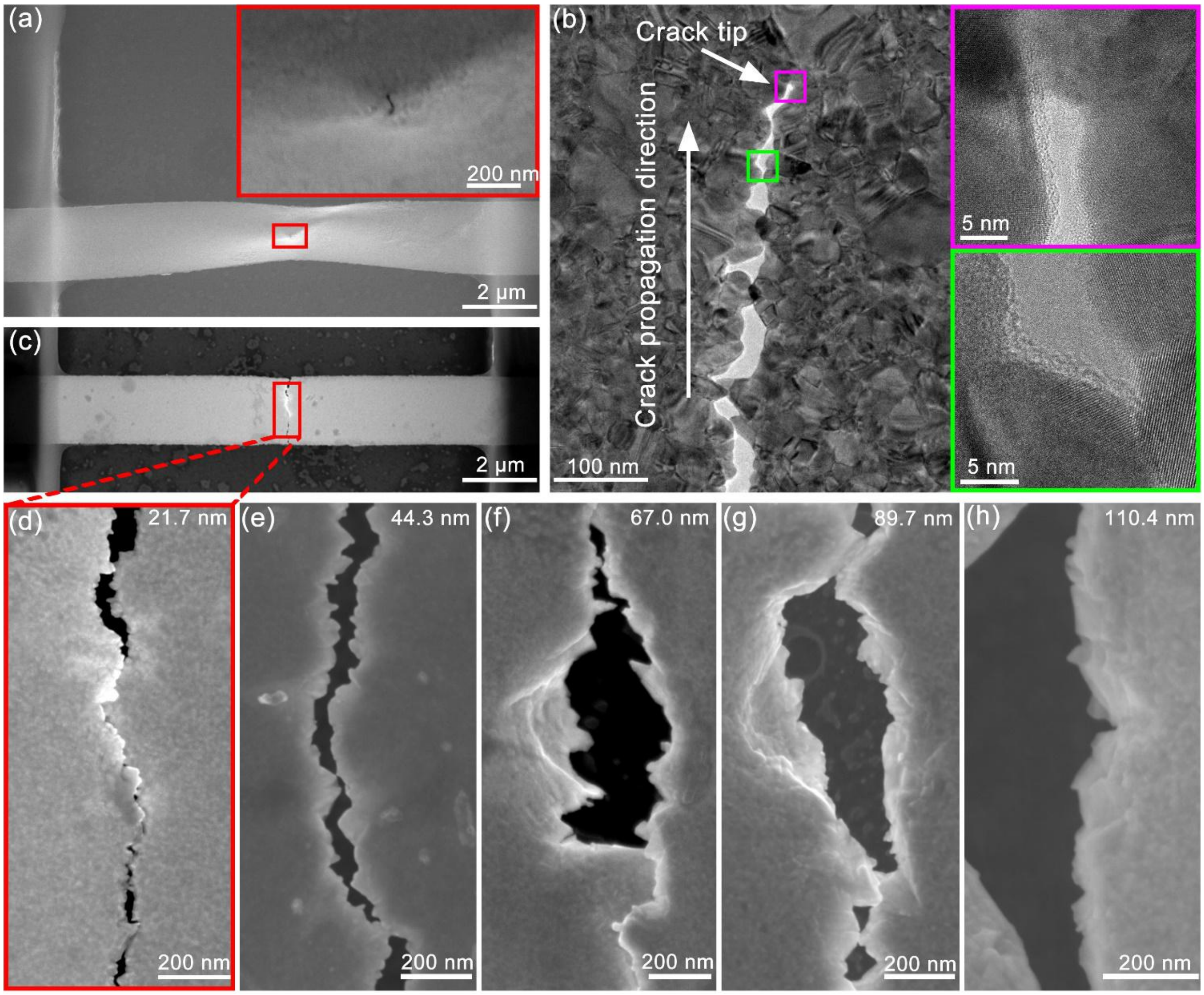

Figure 5 Fracture failure of doubly clamped Au nanobeams under nanoindentation. (a) SEM image of the initial crack for a 21.7 nm thick Au beam. (b) TEM image of crack propagation for a 21.7 nm thick Au beam. (c) SEM image of a completely fractured 21.7 nm thick Au beam. (d-h) SEM images of fractographic features for Au beams with different thicknesses. (d) 21.7 nm, (e) 44.3 nm, (f) 67.0 nm, (g) 89.7 nm, and (h) 110.4 nm.

nanoindentation, the initial crack will extend upward perpendicularly to the upper surface of the nanobeam and eventually form a penetrating crack (Fig. 5(a)). With a further increase in load, the penetrating crack begins to propagate until complete failure. The TEM image shows the crack propagation in the 21.7 nm thick Au film (Fig. 5(b)), and the nanograins on both sides of the crack show obvious complementation and cross-occlusion features. Crack arresting phenomenon is also observed from the crack tip where exists pronounced crack-tip blunting. Some other types of crack arresting are also observed as shown in Fig. S9 in the ESM. SEM image of a complete failure Au nanobeam shows the crack (Fig. 5(c)), and its enlarged SEM image (Fig. 5(d)) shows more details including flat fracture surfaces, complementary sides of the crack, no plastic deformation, and so on, which are very similar to brittle failure. The fracture failure of the 44.3 nm Au beam also presents similar fracture characteristics (Fig. 5(e)). On the contrary, the fracture surfaces of the Au beams with 67.0 nm and larger thicknesses show significant plastic deformation (Figs. 5(f)-5(h)), indicating ductile failure characteristics and higher breaking strength.

For thinner Au nanofilms such as 21.7 nm, the average grain size is close to its thickness, indicating a single-layer grain distribution and low stacking possibility due to dimension limitation in the thickness direction. In this case, the initial crack is more easily to be expanded until complete failure, and the breaking strength is relatively small. For thicker Au nanofilms, grains usually have a multilayer distribution, this can be seen from an obvious lamellar stacking features on the fracture surfaces of the 110.4 nm Au beam (Fig. 5(h)), crackextension will become relatively difficult due to the overlapped grains with random orientation, resulting in a greater breaking strength.

4 Conclusions

In summary, full-spectrum mechanical features of nanocrystalline Au nanofilm with statistical significance, for the first time, have been systematically studied by nanoindentation experiments based on AFM, theoretical analysis, and numerical simulations. The yield and breaking strengths demonstrate strong nonlinear effects different from bulk Au, which might be induced by the coupling effects from nanocrystal size and arrangement limited by nanoscale dimension. As a result, the yield and breaking strengths have a huge increase by nearly an order of magnitude compared to bulk Au and the strong-yield ratio can reach 4, indicating extremely high strength reserve and vibration resistance. But the elastic modulus of the Au nanofilms is approximately the same as that of bulk Au and is almost independent of the thickness and grain size. Interestingly, the Hall-Petch formula can be still valid, but the K nearly raises to twice due to nanoscale effects with respective to bulk nanocrystalline Au. With a decrease in Au nanofilm thickness, the strong-yield ratio gradually decreases, showing a transition from ductile failure to brittle failure. Our results can serve as a benchmark for applications of the Au nanofilms in science research, metering detection, and industry production, and open an effective route for investigating mechanical features of various nanofilms.

5 Method

5.1 Sample preparation

The Au nanofilm beams with 10 μm in length and 2 μm in width were designed and deposited by a magnetron sputtering system (Kurt J. Lesker, PVD 75), and the thickness was controlled by the sputtering time. Restrained by the film formation mechanism of the Physical Vapor Deposition (PVD) method, the minimum film thickness was designed to be about 20 nm to ensure the continuity and flatness of the film samples, and five different thicknesses 21.7 nm, 44.3 nm, 67.0 nm, 89.7 nm, and 110.4 nm (measured by AFM) were prepared. To ensure the doubly-fixed conditions for the two end parts of the beams, the UV photoresist curing method was first developed, so that the unsuspended Au films were strongly attached to the silicon wafer, and the detailed fabrication procedures can be found in the ESM.

5.2 Crystal structure characterizations and calculation of grain size

High-resolution transmission electron microscopy (TEM, FEI, Tecnai G2 F20 U-TWIN) and X-ray diffraction pattern (XRD, Bruker, D8 focus) were utilized to characterize the microstructure of the prepared Au nanobeams. Figures S2(a)-S2(c) show TEM images of Au nanofilms with three thicknesses, which clearly reveal the clustering of individual nanograins. Since it is difficult for transmission electrons of TEM to pass through the Au film with a thickness of 110.4 nm, distinguishing crystal structures in its imaging is almost impossible so it is not shown. Although the grain size distributions of the Au nanofilms with four thicknesses are not uniform, it can be seen that the lateral grain size increases monotonically with the increasing film thickness in plan-view images. Through TEM characterization, the distribution range of in-plane grain sizes in the four-thickness Au nanofilms can be roughly estimated, and the average in-plane grain sizes are calculated, as shown in Fig. 1(d).

The XRD results for Au nanofilms with different thicknesses are shown in Fig. S2(d). where two diffraction peaks of (111) and (222) planes are obtained for all Au nanofilms. The peak intensity increases significantly as the thickness of the Au nanofilm increases. The Scherrer formula is a well-known formula that derives the grain size from the XRD results. When the grain size is smaller than 100 nm, the stress-induced broadening is neglected to grain size-induced broadening, which fulfills the precondition of the Scherrer formula. The average grain size d perpendicular to the Au (111) crystal plane can be expressed as follows.

$$d = \frac{\alpha\gamma}{B\cos\theta} \tag{3}$$

Where γ=1.5405 Å is the X-ray wavelength, α is the Scherrer constant taken as 0.89, B is the half-height width of the diffraction peak and θ is the Bragg diffraction angle of the characteristic peak. As shown in Fig. 1(d), with the increase of the Au nanofilm thickness, the calculated d value increases gradually and is basically within the range of the statistical in-plane grain size. d is relatively lower than the statistical in-plane average grain size because some very small twin boundaries and subgrains are also counted in the calculation.

5.3 AFM probes selection and calibration

To cover the full deformation range of elasticity, plasticity, and failure of Au nanobeams, two probes with different spring constants were selected to fulfill the requirements for load resolution and magnitude at different deformation stages. The indentation force $F = k\Delta D$, where k is the spring constant of the probe rectangular cantilever and ΔD is the bending deflection of the probe. $\Delta D = S\Delta V$, where ΔV is the deflection voltage and S is the deflection sensitivity pre-obtained by the nanoindentation tests on a sapphire substrate. Indentation displacement δ is defined as the deflection of the beam at the indentation location and can be expressed as $\Delta Z - \Delta D$. Under elastic indentation with small deflection, the probe with a standard spring constant $k = 4$ N/m was selected for higher accuracy, while under plastic and failure indentation with large deflection, the probe with a standard spring constant $k = 200$ N/m was selected for higher maximum force. The Sader method, which uses the cantilever dimensions, resonant frequency, and Q-factor [32,34,46] was employed to further calibrate and determine the true spring constant of both probes used. To avoid excessive stress concentration at the indentation position, the diamond-doped probe tip with a diameter of 300 nm was selected and the SEM images of its tip are shown in Fig. S10.

5.4 Nanoindentation measurements

Prior to nanoindentation tests, optical microscope (Olympus OLS4000), SEM (JC-Zeiss, Merlin), and AFM (Bruker, Multimode -8 HR) were used to select the sample without defects and buckling to maintain the accuracy of the nanoindentation, and accurately measure the geometric dimensions of the samples to ensure the accuracy of theoretical calculation. The AFM was used to conduct elastic and plastic nanoindentation tests on Au nanobeams in the air at room temperature. In the elastic stage, the PeakForce Quantitative Nano-Mechanical method (QNM) was adopted where the average tensile strain of the Au nanobeam under nanoindentation was controlled within 0.2%, i.e. the maximum indentation displacement was controlled at about 320 nm. F-δ curves of each Au nanobeam under multiple load cycles were obtained by AFM with gradually increasing loads for each cycle. Plastic nanoindentation experiments were carried out for each thickness of Au nanobeams by means of step-by-step cyclic loading, until the nanobeams were broken, and the breaking loads were recorded. Then 1.5 times the breaking load was used to carry out one-time indentation loading on the Au nanobeam of the same thickness. The Au nanobeam will break, so that the F-δ curve of fracture failure could be obtained. The velocities of the indentation displacements for both experiments were always controlled within 0.3 μm/s, to guarantee the quasi-static loading for each nanoindentation test.

5.5 MD simulation

MD simulations were performed via the large-scale atomic/molecular massively parallel simulator (LAMMPS) code [47] to calculate the elastic modulus and Poisson's ratio of four nanoscale thickness nanocrystalline Au films with five different average grain sizes, and analyze the defect evolution of nanocrystalline Au nanobeams under nanoindentation. Simulation results were visualized and analyzed by the software OVITO [48]. The details of each MD simulation are provided in the Section S4 and S7 in the ESM.

5.6 FEM simulation

The commercial FEM software ANSYS was used to establish a corresponding three-dimensional finite element model according to the geometric dimensions of the Au nanobeam and the spherical probe tip (300 nm diameter). Due to the obvious strain hardening, the bilinear isotropic hardening elastoplastic constitutive model was used to describe the elastic-plastic deformation behavior of the Au nanobeam. This model is described by a bilinear stress-strain curve. The initial slope of the curve is the elastic modulus E. Beyond the specified initial yield stress σ_s, plastic strain develops and the stress-total strain curve continues along a line with slope defined by the specified tangent modulus E_T. The specific finite element modeling, constitutive models, and nanoindentation settings can be seen in the Section S6 in the ESM.

At the same time, to ensure the accuracy of the FEM, mesh independence verification was carried out, as shown in Fig. S7, and the F-δ curves calculated from the higher density meshes were all accorded to the original curve obtained from the initial density mesh.

5.7 Error analysis

In experiments, the measured tip diameter and the calculated prestress may differ slightly from the true-value, thus the F-δ curves under different tip diameters and prestresses were calculated respectively based on FEM to determine the error. Figure S11(a) shows the effects of the tip diameter on the F-δ curves of the Au nanobeam under indentation where the tip diameters are 200, 300, and 400 nm, respectively. When the indentation displacement is less than 600 nm, the obtained F-δ curves are completely coincident, while the displacement exceeds 700 nm, the F-δ curves show slight differences, which originate from the contact nonlinearity between the tip and Au nanobeam. The prestress influences the F-δ responses of the nanobeams in the elastic and plastic stages differently. The FEM based on the plastic model was adopted to compute the F-δ curves of the 21.7 nm thick Au nanobeams under different initial prestresses, as shown in Fig. S11(b) which indicates that Au nanobeam under higher prestress requires greater force for the same displacement. Prestress has a greater influence on the total load when the indentation displacement is small, which is consistent with the conclusion obtained from theoretical analysis based on Eq. (1). When the indentation displacement is greater than 300 nm, the proportions of the forces caused by different prestresses to the total load are much lower. The influences of the prestress and tip diameter on F-δ curves are relatively small in the plastic deformation stage under large displacement nanoindentation. So, the error introduced by the theoretically calculated prestress and the measured tip diameter can be ignored.

Acknowledgements

This work was supported by the National Natural Science Foundation of China (NSFC) (Nos. 51971070), the National Key Research and Development Program of China (No.2016YFA0200403), Eu-FP7 Project (No. 247644), CAS Strategy Pilot Program (No. XRA 09020300). We also appreciate the support in computation experiments from High Performance Computing Center of National Center for Nanoscience and Technology.

Electronic Supplementary Material: Supplementary material (further details of the samples preparations, characterizations, experimental setup, nonlinear mechanical theory analysis, and numerical simulations) is available in the online version of this article at http://dx.doi.org/10.1007/s12274-***-****-*.

References

[1] Hall, E. O. The Deformation and Ageing of Mild Steel: III Discussion of Results. *Proc. Phys. Soc. B* **1951**, *64*, 747.

[2] Petch, N. J iron steel inst. *London* **1953**, *174*, 25-28.

[3] Li, X. Y.; Jin, Z. H.; Zhou, X.; Lu, K. Constrained minimal-interface structures in polycrystalline copper with extremely fine grains. *Science* **2020**, *370*, 831-836.

[4] Hu, J.; Shi, Y. N.; Sauvage, X.; Sha, G.; Lu, K. Grain boundary stability governs hardening and softening in extremely fine nanograined metals. *Science* **2017**, *355*, 1292-1296.

[5] Sun, L. G.; Wu, G.; Wang, Q.; Lu, J. Nanostructural metallic materials: Structures and mechanical properties. *Mater. Today* **2020**, *38*, 114-135.

[6] Zhu, Y. T.; Liao, X. Z.; Wu, X. L. Deformation twinning in nanocrystalline materials. *Prog. Mater. Sci.* **2012**, *57*, 1-62.

[7] Greer, J. R.; De Hosson, J. T. M. Plasticity in small-sized metallic systems: Intrinsic versus extrinsic size effect. *Prog. Mater. Sci.* **2011**, *56*, 654-724.

[8] Pineau, A.; Amine Benzerga, A.; Pardoen, T. Failure of metals III: Fracture and fatigue of nanostructured metallic materials. *Acta. Mater.* **2016**, *107*, 508-544.

[9] Feruz, Y.; Mordehai, D. Towards a universal size-dependent strength of face-centered cubic nanoparticles. *Acta. Mater.* **2016**, *103*, 433-441.

[10] Kondo, M.; Shishido, N.; Kamiya, S.; Kubo, A.;Umeno, Y.; Ishikawa, Y.; Koshizaki, N. High-Strength Sub-Micrometer Spherical Particles Fabricated by Pulsed Laser Melting in Liquid. *Particle & Particle Systems Characterization* **2018**, *35*, 1800061.

[11] Wu, B.; Heidelberg, A.; Boland, J. J. Mechanical properties of ultrahigh-strength gold nanowires. *Nat. Mater.* **2005**, *4*, 525-529.

[12] Calahorra, Y.; Shtempluck, O.;Kotchetkov, V.; Yaish, Y. E. Young's Modulus, Residual Stress, and Crystal Orientation of Doubly Clamped Silicon Nanowire Beams. *Nano Lett.* **2015**, *15*, 2945-2950.

[13] Gao, Y.; Sun, Y.-J.; Zhang, T.-Y. Highly reliable and efficient atomic force microscopy based bending test for assessing Young's modulus of one-dimensional nanomaterials. *Appl. Phys. Lett.* **2016**, *108*, 123104.

[14] Fang, Z.; Geng, Y.; Wang, J.;Yan, Y.; Zhang, G. Mechanical properties of gold nanowires prepared by nanoskiving approach. *Nanoscale* **2020**, *12*, 8194-8199.

[15] Wang, X.; Zheng, S.; Shinzato, S.; Fang, Z.; He, Y.; Zhong, L.; Wang, C.; Ogata, S.; Mao, S. X. Atomistic processes of surface-diffusion-induced abnormal softening in nanoscale metallic crystals. *Nat. Commun.* **2021**, *12*, 5237.

[16] Ramachandramoorthy, R.; Gao, W.; Bernal, R.; Espinosa, H. High Strain Rate Tensile Testing of Silver Nanowires: Rate-Dependent Brittle-to-Ductile Transition. *Nano Lett.* **2016**, *16*, 255-263.

[17] Fu, L.; Kong, D.; Yang, C.; Teng, J.; Lu, Y.; Guo, Y.; Yang, G.; Yan, X.; Liu, P.; Chen, M.; Zhang, Z.; Wang, L.; Han, X. Ultra-high strength yet superplasticity in a hetero-grain-sized nanocrystalline Au nanowire. *Journal of Materials Science & Technology* **2022**, *101*, 95-106.

[18] Liebig, J. P.; Mačković, M.; Spiecker, E.; Göken, M.; Merle, B. Grain boundary mediated plasticity: A blessing for the ductility of metallic thin films? *Acta. Mater.* **2021**, *215*, 117079.

[19] Yan, Y.; Zhao, Y.; Liu, Y. Recent progress in organic field - effect transistor - based integrated circuits. *J. Polym. Sci.* **2021**, *60*, 311-327.

[20] Deal, W.;Mei, X. B.; Leong, K. M. K. H.; Radisic, V.;Sarkozy, S.; Lai, R. THz Monolithic Integrated Circuits Using InP High Electron Mobility Transistors. *IEEE Trans. Terahertz Sci. Technol.* **2011**, *1*, 25-32.

[21] Guo, S.;Wu, K.; Li, C.; Wang, H.; Sun, Z.; Xi, D.; Zhang, S.; Ding, W.; Zaghloul, M. E.; Wang, C.; Castro, F. A.; Yang, D.; Zhao, Y. Integrated contact lens sensor system based on multifunctional ultrathin MoS(2) transistors. *Matter* **2021**, *4*, 969-985.

[22] Gao, L.; Wang, J.; Zhao, Y.; Li, H.; Liu, M.; Ding, J.; Tian, H.; Guan, S.; Fang, Y. Free-Standing Nanofilm Electrode Arrays for Long-Term Stable Neural Interfacings. *Adv. Mater.* **2022**, *34*, e2107343.

[23] Wang, Y.; Liu, Q.; Zhang, J.; Hong, T.; Sun, W.; Tang, L.; Arnold, E.; Suo, Z.; Hong, W.; Ren, Z.; Guo, C. F. Giant Poisson's Effect for Wrinkle-Free Stretchable Transparent Electrodes. *Adv. Mater.* **2019**, *31*, e1902955.

[24] Li, P.; Zhang, Y.; Zheng, Z. Polymer-Assisted Metal Deposition (PAMD) for Flexible and Wearable Electronics: Principle, Materials, Printing, and Devices. *Adv. Mater.* **2019**, *31*, e1902987.

[25] Wang, C.; Wang, C.; Huang, Z.; Xu, S. Materials and Structures toward Soft Electronics. *Adv. Mater.* **2018**, *30*, e1801368.

[26] Erdogan, R. T.; Alkhaled, M.; Kaynak, B. E.; Alhmoud, H.; Pisheh, H. S.; Kelleci, M.; Karakurt, I.; Yanik, C.; Sen, Z. B.; Sari, B.; Yagci, A. M.; Ozkul, A.; Hanay, M. S. Atmospheric Pressure Mass Spectrometry of Single Viruses and Nanoparticles by Nanoelectromechanical Systems. *ACS Nano* **2022**, *16*, 3821-3833.

[27] Xu, B.; Zhang, P.; Zhu, J.; Liu, Z.; Eichler, A.; Zheng, X. Q.; Lee, J.; Dash, A.; More, S.; Wu, S.; Wang, Y.; Jia, H.; Naik, A.; Bachtold, A.; Yang, R.; Feng, P. X.; Wang, Z. Nanomechanical Resonators: Toward Atomic Scale. *ACS Nano* **2022**, *16*, 15545-15585.

[28] Luo, J.; Liu, S.; Chen, P.; Chen, Y.; Zhong, J.; Wang, Y. Highly Sensitive Hydrogen Sensor Based on an Optical Driven Nanofilm Resonator. *ACS Appl. Mater. Interfaces* **2022**, *14*, 29357-29365.

[29] Eom, K.; Park, H. S.; Yoon, D. S.; Kwon, T. Nanomechanical resonators and their applications in biological/chemical detection: Nanomechanics principles. *Phys. Rep.* **2011**, *503*, 115-163.

[30] Gleiter, H. Nanostructured materials: Basic concepts and microstructure. *Acta. Mater.* **2000**, *48*, 1-29.

[31] Meyers, M. A.; Mishra, A.; Benson, D. J. Mechanical properties of nanocrystalline materials. *Prog. Mater. Sci.* **2006**, *51*, 427-556.

[32] Lee, C.; Wei, X.; Kysar, J. W.; Hone, J. Measurement of the elastic properties and intrinsic strength of monolayer graphene. *Science* **2008**, *321*, 385-388.

[33] Lee, G.-H.; Cooper, R. C.; An, S. J.; Lee, S.; van der Zande, A.; Petrone, N.; Hammerberg, A. G.; Lee, C.; Crawford, B.; Oliver, W.; Kysar, J. W.; Hone, J. High-Strength Chemical-Vapor-Deposited Graphene and Grain Boundaries. *Science* **2013**, *340*, 1073-1076.

[34] Sun, Y.; Wang, Y.; Wang, E.; Wang, B.; Zhao, H.; Zeng, Y.; Zhang, Q.; Wu, Y.; Gu, L.; Li, X.; Liu, K. Determining the interlayer shearing in twisted bilayer MoS2 by nanoindentation. *Nat. Commun.* **2022**, *13*, 3898.

[35] Patterson, A. L. The Scherrer Formula for X-Ray Particle Size Determination. *Phys. Rev.* **1939**, *56*, 978-982.

[36] Rui, Z.; Rebecca, C. Mechanical Properties and Applications of Two-Dimensional Materials. In *Two-dimensional Materials*. N. Pramoda Kumar, Ed.; IntechOpen; Rijeka, 2016; pp Ch. 10.

[37] Li, P.; You, Z.; Haugstad, G.; Cui, T. Graphene fixed-end beam arrays based on mechanical exfoliation. *Appl. Phys. Lett.* **2011**, *98*, 253105.

[38] Dang, C.; Chou, J.-P.; Dai, B.; Chou, C.-T.; Yang, Y.; Fan, R.; Lin, W.; Meng, F.; Hu, A.; Zhu, J.; Han, J.; Minor, A. M.; Li, J.; Lu, Y. Achieving large uniform tensile elasticity in microfabricated diamond. *Science* **2021**, *371*, 76-78.

[39] Banerjee, A.; Bernoulli, D.; Zhang, H.; Yuen, M.-F.; Liu, J.; Dong, J.; Ding, F.; Lu, J.; Dao, M.; Zhang, W.; Lu, Y.; Suresh, S. Ultralarge elastic deformation of nanoscale diamond. *Science* **2018**, *360*, 300-302.

[40] Yu, Q.; Zhang, J.; Li, J.; Wang, T.; Park, M.; He, Q.; Zhang, Z.; Liang, T.; Ding, X.; Li, Y. Y.; Wang, Q.; Zeng, Q.; Yang, Y. Strong, Ductile, and Tough Nanocrystal-Assembled Freestanding Gold Nanosheets. *Nano Lett.* **2022**, *22*, 822-829.

[41] Espinosa, H. Plasticity size effects in free-standing submicron polycrystalline FCC films subjected to pure tension. *J. Mech. Phys. Solids* **2004**, *52*, 667-689.

[42] Naik, S. N.; Walley, S. M. The Hall–Petch and inverse Hall–Petch relations and the hardness of nanocrystalline metals. *J. Mater. Sci.* **2020**, 55, 2661-2681.

[43] Cordero, Z. C.; Knight, B. E.; Schuh, C. A. Six decades of the Hall–Petch effect – a survey of grain-size strengthening studies on pure metals. *Int. Mater. Rev.* **2016**, *61*, 495-512.

[44] Carlton, C. E.; Ferreira, P. J. What is behind the inverse Hall–Petch effect in nanocrystalline materials? *Acta. Mater.* **2007**, *55*, 3749-3756.

[45] Hahn, E. N.; Meyers, M. A. Grain-size dependent mechanical behavior of nanocrystalline metals. *Mater. Sci. Eng. A* **2015**, *646*, 101-134.

[46] Sader, J. E.; Chon, J. W. M.; Mulvaney, P. Calibration of rectangular atomic force microscope cantilevers. *Rev. Sci. Instrum.* **1999**, *70*, 3967-3969.

[47] Plimpton, S. Fast Parallel Algorithms for Short-Range Molecular Dynamics. *J. Comput. Phys.* **1995**, *117*, 1-19.

[48] Stukowski, A. Visualization and analysis of atomistic simulation data with OVITO–the Open Visualization Tool. *Modelling Simul. Mater. Sci. Eng.* **2010**, *18*, 015012.

Electronic Supplementary Material

Dimension-dependent mechanical features of Au Nanocrystalline nanofilms

Lijun Ma[1,2,§], Lena Du[3,§], Shu Wang[2], Qing Wang[6], Shifeng Xue[1](✉), Hanxing Zhu[4](✉), and Qian Liu[2,5](✉)

[1] *Department of Engineering Mechanics, College of Pipeline and Civil Engineering, China University of Petroleum (East China), Qingdao 266580, China*

[2] *CAS Center for Excellence in Nanoscience, National Center for Nanoscience and Technology & University of Chinese Academy of Sciences, Beijing 100190, China*

[3] *Department of Physics, Capital Normal University, Beijing 100048, China*

[4] *School of Engineering, Cardiff University, Cardiff CF24 3AA, UK*

[5] *MOE Key Laboratory of Weak-Light Nonlinear Photonics, TEDA Applied Physics Institute, School of Physics, Nankai University, Tianjin 300457, China*

[6] *College of Mechanical and Architectural Engineering, Taishan University, Tai'an 271000, China*

§ *These authors contributed equally*

Supporting information to DOI 10.1007/s12274-****-****-*

Address correspondence to Qian Liu, liuq@nanoctr.cn; Hanxing Zhu, zhuh3@cardiff.ac.uk; Shifeng Xue, sfeng@upc.edu.cn

S1 Preparation of suspended Au nanofilm beams

In this study, a large-scale array of double-clamped suspended Au nanobeams was designed and fabricated. The fabrication procedure of the large-scale doubly clamped Au nanobeam array is shown in Fig. S1. Firstly, based on the micro-nano processing method, Au nanofilms with nanocrystalline were prepared on the cleaned glass substrate surface through a series of processes such as photolithography, deposition, and degumming. A magnetron sputtering instrument (Kurt J. Lesker, PVD 75) was used to deposit Au nanofilms with different thicknesses, and the thickness was controlled by the sputtering time. The Au target with a purity of 99.999% was selected as the target material. Restrained by the film formation mechanism of the Physical Vapor Deposition (PVD) method, the minimum film thickness was designed to be about 20 nm to ensure the continuity and flatness of the film samples, and five different thicknesses 21.7 nm, 44.3 nm, 67.0 nm, 89.7 nm, and 110.4 nm (measured by AFM) were prepared. The trenches with a width of about 10 um and a depth of about 3 μm were prepared on the surface of the cleaned silicon wafer through the processes of photolithography, etching, and degumming. Then, ultraviolet (UV) curable adhesive (Norland Optical Adhesive NOA 61) was uniformly spin-coated on the surface of the silicon wafer with trenches. Due to the surface tension of the UV curable adhesion, it was not easy to flow into the trench and was mainly coated on the silicon wafer surface. By using a high-precision alignment transfer system (Film Aligner and Transfer System, Shanghai Onway Technology Co., Ltd), the glass substrate processed with the Au nanobeam array was aligned and attached to the silicon wafer surface with adhesion. The UV curable adhesion was exposed to the UV light (365 nm, 200 W) for 30 minutes until fully cured to obtain strong adhesion and corrosion resistance. In this way, all the Au nanofilms except the suspended Au beams on the upper of the trenches were strongly bonded to the silicon wafer surface. Subsequently, the glass substrate was removed by wet etching with 4% hydrofluoric acid for 20 minutes, and a large-scale array of suspended Au nanobeams clamped at both ends was obtained. Finally, after 1 week of aging, chemical bonds were formed between the Au nanofilms, the cured adhesive, and the silicon wafer, so that the best bonding quality between the Au nanofilm and silicon wafer was achieved. The prepared Au nanobeams with about 10 μm in length and 2 μm in width show high stability under large displacement nanoindentation based on the atomic force microscope (AFM, Bruker, Multimode -8 HR), which can be used for convenient and accurate nanoindentation experiments.

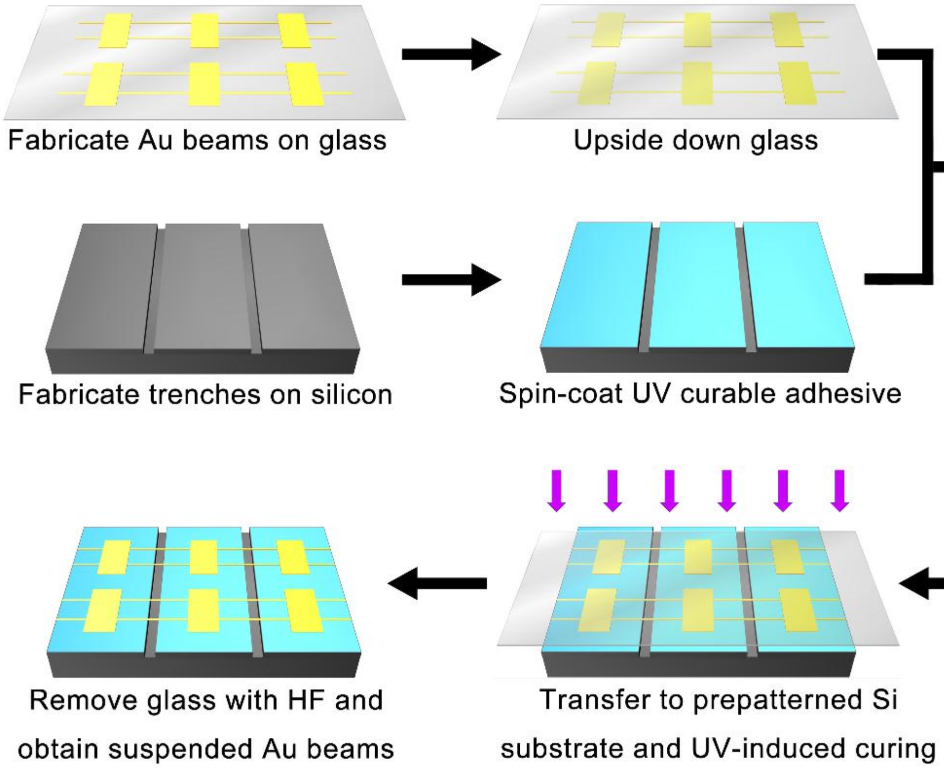
Fabricate Au beams on glass
Upside down glass
Fabricate trenches on silicon
Spin-coat UV curable adhesive
Remove glass with HF and obtain suspended Au beams
Transfer to prepatterned Si substrate and UV-induced curing

Figure S1 The fabrication procedure of doubly clamped gold (Au) nanobeams with nanocrystalline.

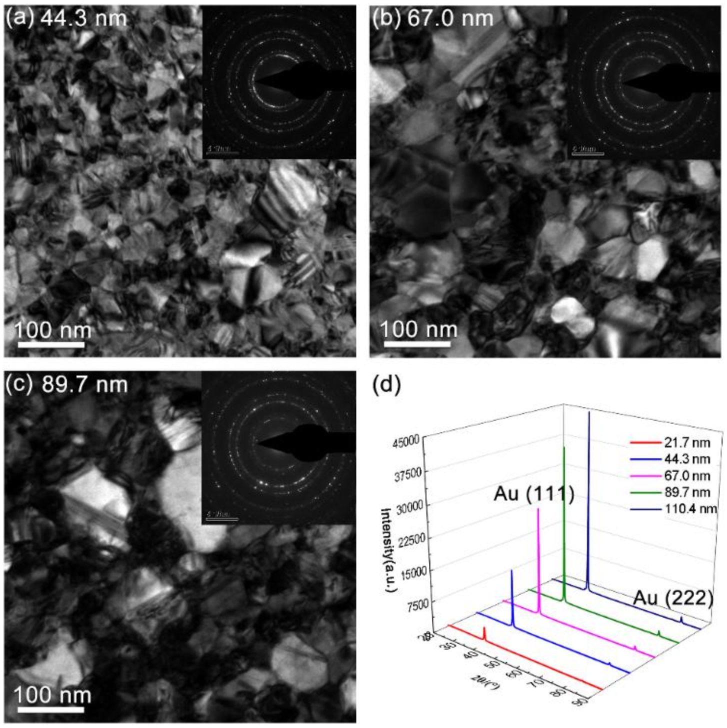
(a) 44.3 nm
100 nm
(b) 67.0 nm
100 nm
(c) 89.7 nm
100 nm
(d)
45000
37500
30000
22500
15000
7500
Intensity(a.u.)
30
40
50
60
70
80
90
2θ(°)
Au (111)
Au (222)
21.7 nm
44.3 nm
67.0 nm
89.7 nm
110.4 nm

Figure S2 TEM bright-field images and the constituency electron diffraction patterns of Au nanofilms with different thicknesses. (a) 44.3 nm, (b) 67.0 nm, and (c) 89.7nm. (d) XRD of Au nanofilms with different thicknesses.

S2 A detailed description of the non-linear elastic continuum mechanics model

Although the deformation of Au nanobeam under nanoindentation was always controlled in the elastic stage, the deflection in the midpoint of the Au nanobeam was much larger than its thickness. The large deflection increased the rigidity of doubly-clamped nanobeams, which made the F-δ response exhibit geometric nonlinearity (Fig. 2(a)). A nonlinear elastic continuum mechanics model (S1)[1,2] derived based on the variational method, considering geometric nonlinearity and initial stress (i.e. prestress), is introduced to describe the force-displacement relationship of the Au nanobeams.

$$F = F_{ben} + F_{pre} + F_{ten} = 16Ew\left(\frac{t}{l}\right)^3\delta + \sigma_0 t\delta + \frac{8}{3}Ewt\left(\frac{\delta}{l}\right)^3 \tag{S1}$$

Where F_{ben} represents the contribution of linear elastic bending to the total load, F_{pre} represents the contribution of the prestress to the total load, and F_{ten} represents the contribution of the additional axial tension induced by the large deformation to the total load. This theoretical model shows that the contributions of these three terms to the total load vary with indentation displacement and the thickness of the Au nanobeam. Differentiating from the traditional bending theory which does not consider prestress and large deformation, this model takes into account the stiffness enhancement caused by the prestress and additional tension which greatly improves the load bearing capacity before plastic deformation and failure of the Au nanobeam. Figure S3 shows the contributions of these three terms to the total load with the increasing indentation displacement of Au nanobeams with different thicknesses. The contribution of prestress to the total load is obvious at small displacement and gradually decreases with the increase of thickness, while the contribution of linear elastic bending is just the opposite. When the thickness reaches 110.4 nm (Fig. S3), the linear elastic bending dominates the total load at a small displacement. The indentation load is mainly borne by the flexural rigidity and prestress of the beam when the indentation displacement is small. When the indentation displacement increases, the contributions of prestress and linear elastic bending to the total load decrease monotonously, while the contribution of the additional axial tension to the total load increases monotonously which exceeds the former two for all Au beams. The load-bearing mechanism of the beam gradually changes from the bending-dominated mode to the tensile-dominant mode with the increase of the indentation displacement, showing a typical geometric nonlinear elastic effect under large elastic deformation.

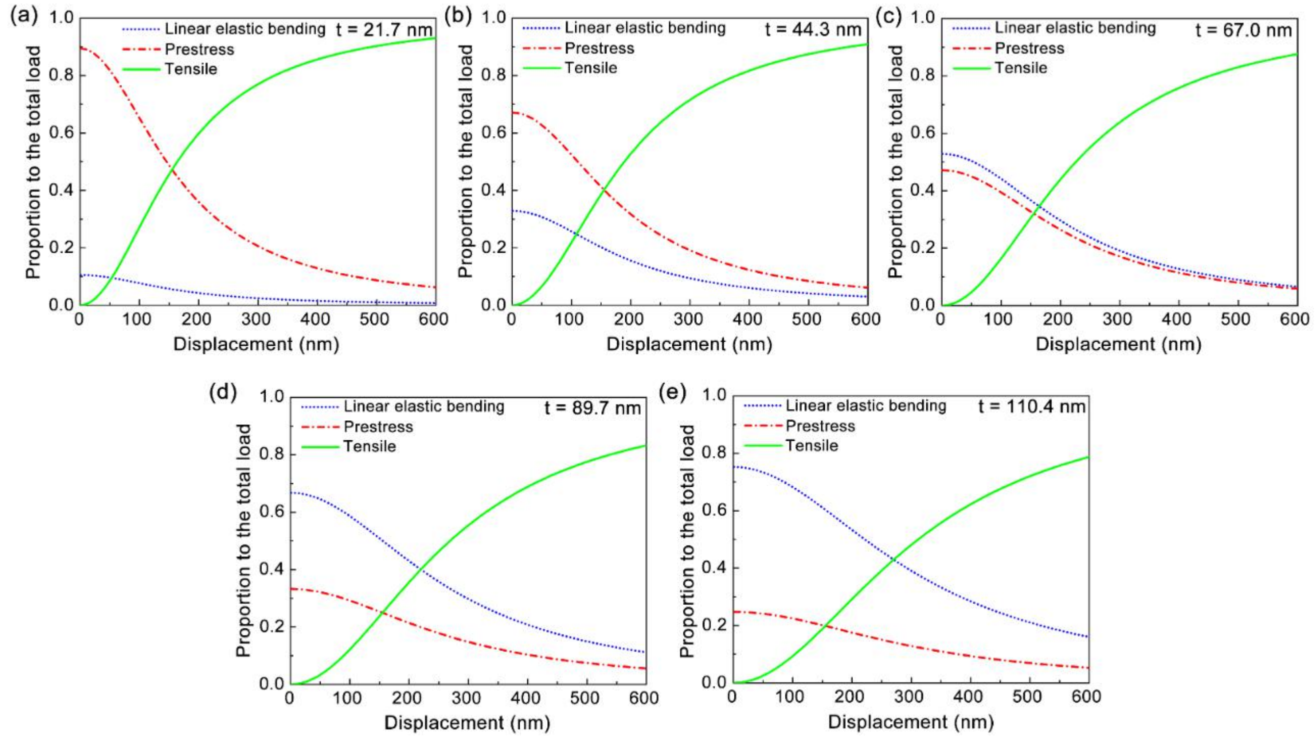

Figure S3 The contributions proportion of linear elastic bending, prestress, and tension to the total load with the increase of indentation displacement. (a) 21.7 nm, (b) 44.3 nm, (c) 67.0 nm, (d) 89.7 nm, and (e) 110.4 nm.

S3 Statistical results for elastic modulus and prestress

The elastic modulus and prestress of the 44.3 nm, 67.0 nm, 89.7 nm, and 110.4 nm thick Au beams are shown in Fig. S4. The statistical results of the elastic modulus show the well-fitted Gaussian distributions for the Au nanobeams with different thicknesses, and the average values of the elastic moduli of different thick nanobeams are basically consistent within 75-80 GPa. This indicates that the elastic modulus of the Au nanobeams does not change with the thickness. The distribution of prestress is slightly scattered which is mainly because the prestress is randomly introduced during the processing and transferring of the Au nanobeams. Meanwhile, the statistical results of the prestress also show the fitted Gaussian distributions for nanobeams with different thicknesses, which is mainly because the Au nanobeams with the same thickness are processed and transferred at one time. The stress states in the doubly clamped Au nanobeams can be divided into three types: tensile stress state, compressive stress state, and stress-free state. The stress-free state is where the prestress of the nanobeam is 0, which is an ideal state, and only a few beams are in the stress-free state. The tensile stress state means the prestress is positive and the nanobeam is in the pretension state, which enhances the flexural rigidity. The compressive stress state is that the prestress is negative, and the nanobeam is in the axial compression state. When the compressive prestress is small, the Au nanobeam can maintain the original geometry. However, when the compressive prestress is large and exceeds the critical buckling stress of the suspended Au nanobeam, buckling instability will occur, resulting in upward or downward bending. Each Au nanobeam has been characterized and screened to ensure that the nanobeam is not buckled before the indentation test, thus the compressive prestress for calculation will not exceed its critical buckling stress. The rationality of the prestress results from the theoretical model and experiments can be verified in Note S4.

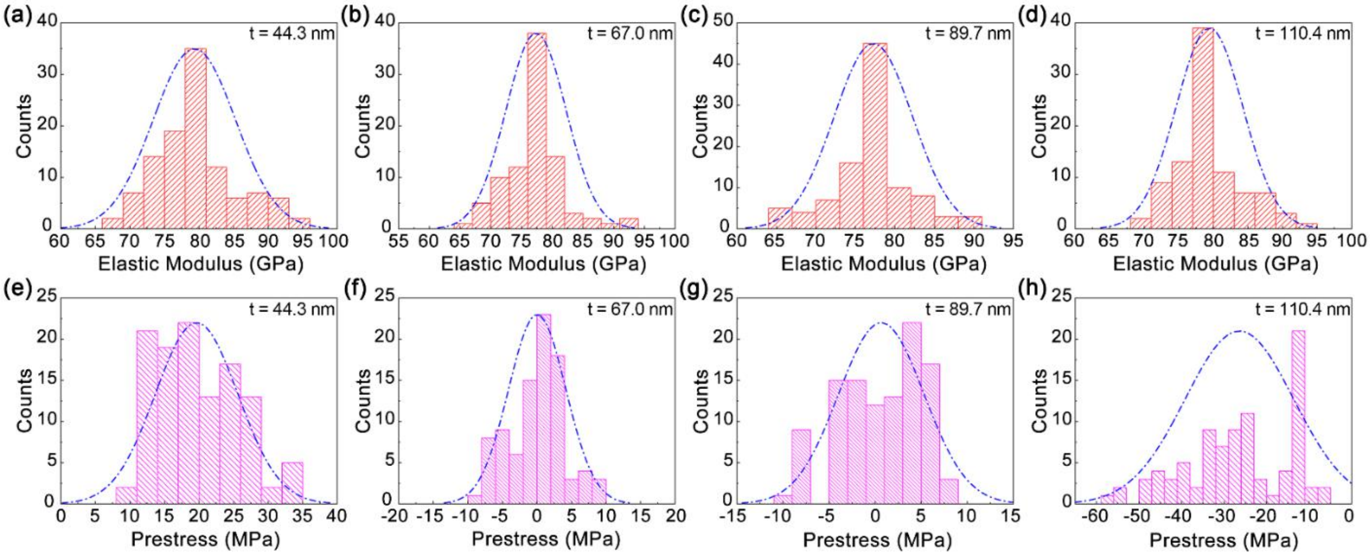

Figure S4 Statistical results of elastic modulus and prestress. (a-d) The histograms of elastic modulus for (a) 44.3 nm, (b) 67.0 nm, (c) 89.7 nm, and (d) 110.4 nm thick Au beam. (e-h) The histograms of prestress for (e) 44.3 nm, (f) 67.0 nm, (g) 89.7 nm, and (h) 110.4 nm thick Au beam. The blue dot-dash lines indicate the fitted Gaussian distributions.

S4 Molecular dynamic (MD) simulation for computing the elastic constants

Unlike anisotropic single crystal, the polycrystalline is generally isotropic due to the arbitrary orientation of grains and the elastic constants in each direction are similar. To accurately calculate the elastic modulus and Poisson's ratio of Au films with different nanoscale thicknesses and nanograin sizes, MD simulation was used to first compute the elastic constant tensor.

The MD simulations were performed using the Large-Scale Atomic/Molecular Massively Parallel Simulator (LAMMPS) code.[3] Since only the thickness (z) dimension of the Au nanobeams measured experimentally is in the nanoscale, and the length (x direction) and width (y direction) are in the microscale, a microelement of the Au nanobeam is taken as the research object. Considering the surface effects, periodic boundary conditions were imposed in the x and y directions, and free boundary conditions were applied in the z direction. The length and width of the microelement are 40 nm, and the thicknesses of the microelement in the z direction were set to 20 nm, 40 nm, 60 nm, and 80 nm, respectively. Microelement models with mean grain sizes of 7 nm, 11 nm, 15 nm, 19 nm, and 23 nm for each thickness, respectively, were constructed by using the Atomsk program based on the Voronoi tessellation method.[4] The lattice orientation and position of grains were randomly selected and the MD models and results were visualized and analyzed by software OVITO.[5] Figure 2(e) shows the MD model with an average grain size of 15 nm and a thickness of 40 nm whose corresponding atomic structure images were rendered by common neighbor analysis (CAN).[6] Blue atoms represent the face-centered cubic (FCC) structure, and the rest of the atoms represent the grain boundary. The embedded atom method (EAM) potential developed by Foiles et al.[7] was utilized to determine the interatomic potential of the Au-Au where the total energy E for a system includes the pairwise potential and the many-body embedding energy, and can be written as:

$$E_{tot} = \sum_i F_i\left(\sum_{i\neq j} \rho_j(r_{ij})\right) + \frac{1}{2}\sum_{i,j(i\neq j)} \emptyset_{ij}(r_{ij}) \tag{S2}$$

where F_i is the embedding energy of atom i, ρ_j is the spherically averaged atomic electron density, $\emptyset_{ij}$ is the pairwise interaction function between atoms i and j, and r_{ij} is the distance between atoms i and j. The NVE ensemble was adopted to keep the number of atoms, the volume, and the energy of the models unchanged, and all atoms were kept at 300 K with the Langevin thermostat as thermostat atoms during deformation. 0.1% tension, compression, or shear strain was applied to the model box in the x, y, z, xy, xz, or yz directions to calculate the elasticity constants. To ensure the correctness of the elastic constants, whether the MD sampling of stress components is generating accurate statistical averages must be verified. The average elastic modulus E and Poisson's ratio ν can be computed approximately with the Voigt-Reuss-Hill averaging rule[8] for Au. According to the symmetry of the FCC structure, Au has 3 independent elasticity coefficients (C_{11}, C_{12}, C_{44}).

The Voigt-averaging rule:[9]

$$\text{Bulk modulus } B_V = \frac{C_{11}+2C_{12}}{3} \tag{S3}$$

$$\text{Shear modulus } G_V = \frac{C_{11}-C_{12}+3C_{44}}{5} \tag{S4}$$

The Reuss-averaging rule:[10]

$$\text{Bulk modulus } B_R = \frac{C_{11}+2C_{12}}{3} \tag{S5}$$

$$\text{Shear modulus } G_R = \frac{5(C_{11}-C_{12})C_{44}}{3(C_{11}-C_{12})+4C_{44}} \tag{S6}$$

Voigt-Reuss-Hill averaging rule:[8]

$$\text{Bulk modulus } B_H = \frac{B_V+B_R}{2} \tag{S7}$$

$$\text{Shear modulus } G_H = \frac{G_V+G_R}{2} \tag{S8}$$

$$\text{Young's modulus } E = \frac{9B_H G_H}{3B_H+G_H} \tag{S9}$$

$$\text{Poisson ratio } \nu = \frac{3B_H-2G_H}{2(3B_H+G_H)} \tag{S10}$$

Based on MD and the Voigt-Reuss-Hill averaging rule, the elastic modulus and Poisson's ratio of Au nanofilms with different grain sizes and thicknesses can be obtained, as shown in Fig. 2(f). The results show that the elastic modulus and Poisson's ratio are basically steady as the thickness increases for Au nanofilms. In addition, with the increase of the nanograin size, the elastic modulus initially increases slightly and then tends to be stable, which is basically in the range of 75-80 GPa. The Poisson's ratio is always stable at about 0.42.

S5 Rationality verification of prestress based on the buckling theory

According to the buckling theory of beams, the critical buckling load and critical buckling stress of the doubly clamped Au nanobeam can be estimated approximately by using the Euler formula, so that the rationality of the prestress results from the theoretical model and experiments can be verified. The critical compressive buckling stress is given by the following formula

$$\sigma_{cr} = \frac{\pi^2 EI}{(\mu l)^2 A} \tag{S11}$$

When both ends of the beam are clamped, μ is taken as 0.5, I is the section moment of inertia, A is the cross-sectional area, and l is the length of the Au nanobeam. When the cross-section is a rectangle, $I = bt^3/12$ and $A = bt$, where b and t are the width and thickness of the nanobeam cross-section, respectively. In order to simplify the computational process, the length and width of the Au nanobeam here are uniformly taken as the design dimensions of the Au nanobeams. The relationship between the critical buckling stress and the thickness of the Au nanobeams is shown in Fig. S5. The prestress values of all the 21.7 nm and 44.3 nm thick Au beams are greater than 0, indicating a pretension stress state. The prestresses of some 67.0 and 89.7 nm thick Au beams are less than 0, but none reaches the corresponding critical buckling stress. Therefore, the calculated prestress satisfies the stress state of the Au nanobeams screened according to the condition of no buckling. However, the prestress values of a few 110.4 nm thick Au nanobeams exceed the corresponding critical buckling stress, but the excess part is within a reasonable error range due to the influence of errors in the theoretical model, geometric dimensions, and experimental measurements. The prestress values of nanocrystalline Au beams calculated based on the theoretical model and experimental measurements are credible from the perspective of critical buckling stress.

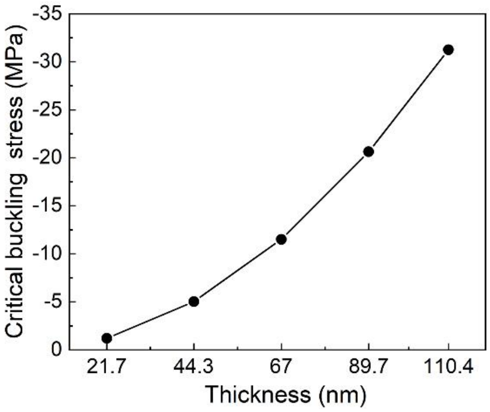

Figure S5 The critical buckling stress vs. the thicknesses of Au nanobeams.

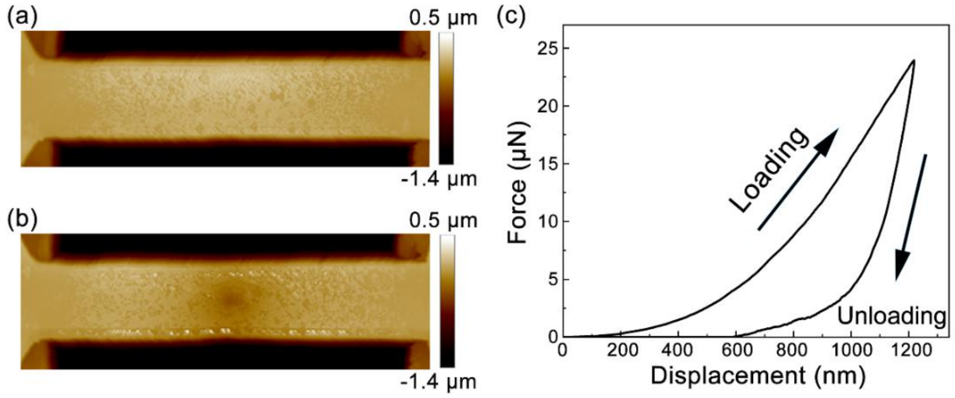

Figure S6 Plastic deformation of 44.3 nm thick Au beam under indentation. (a and b) The AFM images of the Au nanobeam (a) before and (b) after indentation. (c) The F-δ curve during loading and unloading.

S6 Finite element simulation (FEM) for nanoindentation

Numerical simulations based on FEM were conducted using the commercial finite element software ANSYS. Using SOLID186 elements (3-D 20-Node homogeneous Structural Solid), the three-dimensional Au nanobeam models were established according to the real geometric dimensions. A rigid hemispherical diamond tip model with 300 nm diameter was established above the middle of the nanobeam using SOLID187 elements (3-D 10-Node tetrahedral Structural Solid). Due to the obvious strain hardening, the bilinear isotropic hardening elastoplastic constitutive model (plastic model) was employed to describe the stress-strain (σ-ε) relationship of Au nanobeams under elastic-plastic nanoindentation. This model mainly includes five mechanical parameters, namely the elastic modulus *E*, Poisson's ratio *v*, the yield strength σ_s, the yield strain ε_s, and the tangent modulus E_T, and the simplified model form is as follows.

$$\sigma = \begin{cases} E\varepsilon & \varepsilon \le \varepsilon_s \\ \sigma_s + E_T(\varepsilon - \varepsilon_s) & \varepsilon > \varepsilon_s \end{cases} \tag{S12}$$

For further confirmation, an ideal linear elastic constitutive model (elastic model) was employed. The elastic model mainly includes the elastic modulus *E* and Poisson's ratio *v*. According to the experimental results, the *E* of models was set as 78 GPa. The *v* was adopted as 0.42 calculated by MD simulations in the previous section and the E_T was generally taken as *E*/20-*E*/10 GPa. To ensure the FEM results match the experimental *F*-δ curves, the E_T was taken as 5 GPa. Before indentation, the average prestress calculated theoretically was introduced by pre-stretching the Au nanobeam. As the nanobeams were clamped at both ends, all the nodes on the two edges of the nanobeams were fixed in all FEM simulations. Meanwhile, the x and y displacements of the indenter tip were restrained, the contact condition between the tip and beam was defined as frictionless and finite slip was allowed. An indentation displacement of 1000 nm in the z direction was applied on the indenter tip for the incremental loading with 300 substeps. For the applied z-displacements on the indenter tip, the corresponding forces can be obtained. According to the strength theory, the maximum distortion energy density theory was used to evaluate the yield and breaking strength of the Au nanobeam. The equivalent stress (Von Mises stress, $\overline{\sigma}$) can be expressed as follows.

$$\overline{\sigma} = \frac{1}{\sqrt{2}}\sqrt{\left(\sigma_{xx}-\sigma_{yy}\right)^2 + (\sigma_{xx}-\sigma_{zz})^2 + \left(\sigma_{yy}-\sigma_{zz}\right)^2 + 6\left(\sigma_{xy}^2+\sigma_{xz}^2+\sigma_{yz}^2\right)} \tag{S13}$$

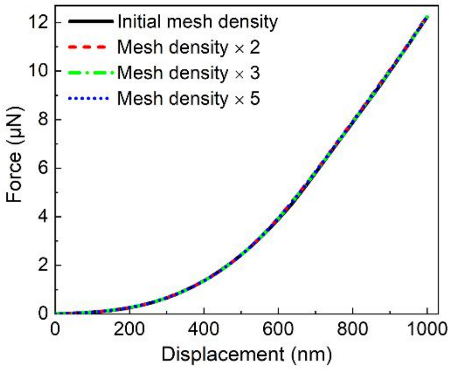

Figure S7 The *F*-δ curves obtained from the Au nanobeam finite element model with different mesh densities.

S7 MD simulation for nanoindentation

MD simulation using the software LAMMPS was adopted to further understand the deformation process of the Au nanobeam with nanocrystalline under nanoindentation. A nanocrystalline Au nanobeam with a size of 100 × 20 × 2 nm^3 containing 235580 atoms was constructed using the Atomsk program, in which the average two-dimensional grain size is about 10 nm. The EAM potential developed by Foiles et al.[7] was used to describe the interactions between Au atoms. A spherical tip with the diamond cubic lattice structure and a 3 nm diameter was placed above the middle of the Au nanobeam. The Tersoff potential[11] was used to describe the interactions between carbon atoms in the diamond tip. The interaction between the Au atoms and the carbon atoms can be described by the pairwise Morse potential:

$$U = D\{\exp[-2\alpha(r_{ij} - r_0)] - 2\exp[-\alpha(r_{ij} - r_0)]\} \tag{S14}$$

Where D is the cohesion energy, α is a constant parameter fitted to the bulk modulus of the material, r_{ij} is the separation distance between atoms i and j, and r_0 is the distance at equilibrium. The morse potential parameters were selected from the reference.[12] The non-periodic boundary conditions were adopted in all directions. Before indentation, energy minimization was first performed to optimize atomic configuration using the conjugate gradient algorithm. Atoms at both ends of the suspended nanobeam were frozen by setting the velocities and forces as constant zero, which served as boundary atoms. The rest of the Au atoms were relaxed using the canonical (NVT) ensemble (constant number of atoms, volume, and temperature) to reach a thermal equilibrium state for 30 picoseconds (ps). To exclude the effects of random vibration of atoms and more clearly observe defect evolution, MD simulation was carried out at 100 K which was maintained by the Nosé-Hoover thermostat.[13,14] Time step was set as 1 femtosecond where the NVT ensemble was used to perform time integration on the Nosé-Hoover style non-Hamiltonian equations of motion, and the position and velocity of Au atoms were updated each timestep. During the indentation, the spherical diamond tip moved downwards along the Z direction at a constant speed of 0.1 Å/ps with 2000 ps indentation time, so the corresponding maximum indentation displacement was 200 Å. The NVE ensemble was adopted to keep the number of atoms, the volume, and the energy of models unchanged, and all atoms were kept at 100 K with the Langevin thermostat during indentation.

A 10 nm thick slice perpendicular to the z-axis was made and visualized using the software OVITO to track the defect evolution of nanocrystalline Au nanobeam under nanoindentation (Fig. S8(a)). Atoms were rendered according to CNA, where green, white, and red colors represent atoms in FCC structure, grain boundary, and dislocation, respectively. To better observe defect generation and evolution, atoms in the FCC structure colored green and the tip were removed, atoms in grain boundary colored white, and dislocations colored red are shown in Figs. S8(b)-S8(f). With the increase of indentation displacement, dislocation sources first nucleate at the grain boundary, as shown by the cyan ellipse in Figs. S8(c) and S8(d). Dislocations in the grain are shown by the green ellipse in Fig. S8(e). Dislocations penetrating the whole grain tend to form a pile-up group, significantly strengthening the crystals, as shown by the pink ellipse in Fig. S8(f). Massive dislocations initiated in grains near the indenter result in dislocation slip, grain boundary sliding, and grain rotation, as shown by the blue rectangles in Figs. S8(b) and S8(d) both contribute to plastic deformation.

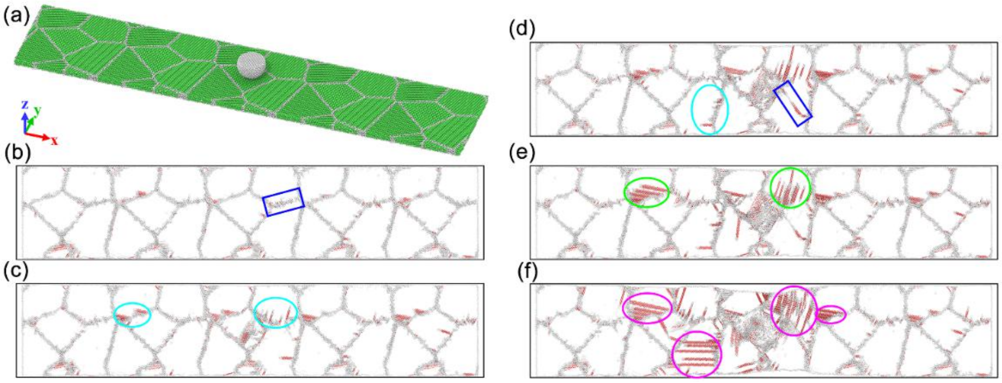

Figure S8 The MD simulation and defect evolution of the doubly clamped nanocrystalline Au beam under nanoindentation. (a) Perspective view of a 10 nm thick slice perpendicular to the z-axis. (b-f) Defect evolution analysis under indentation displacements of (b) 0 nm, (c) 2.5 nm, (d) 4.5 nm, (e) 5.5 nm, and (f) 11 nm.

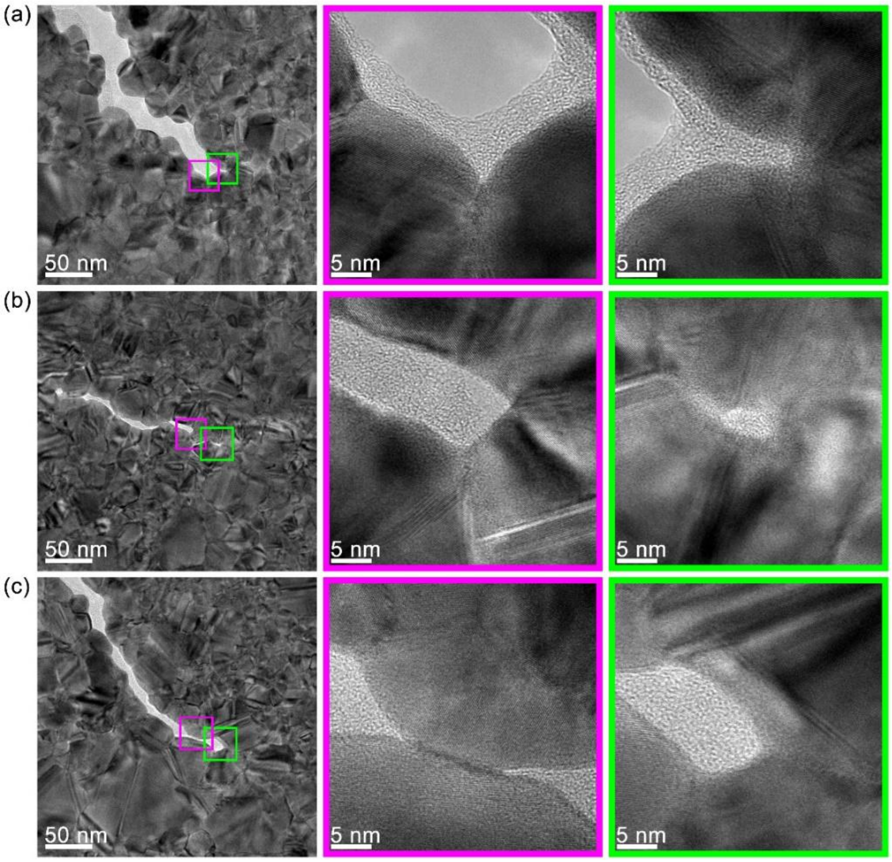

Figure S9 TEM images of the crack tip and propagation of a 21.7 nm thick Au beam. (a) The crack arresting occurs at the junction of three grains, and the crack tip presents obvious bluntness. (b) The crack arresting occurs at the junction of three grains, and the crack tip presents obvious bluntness. A hole appears in front of the crack tip. (c) The crack propagates along the grain boundary near the crack tip and stops at the grain boundary.

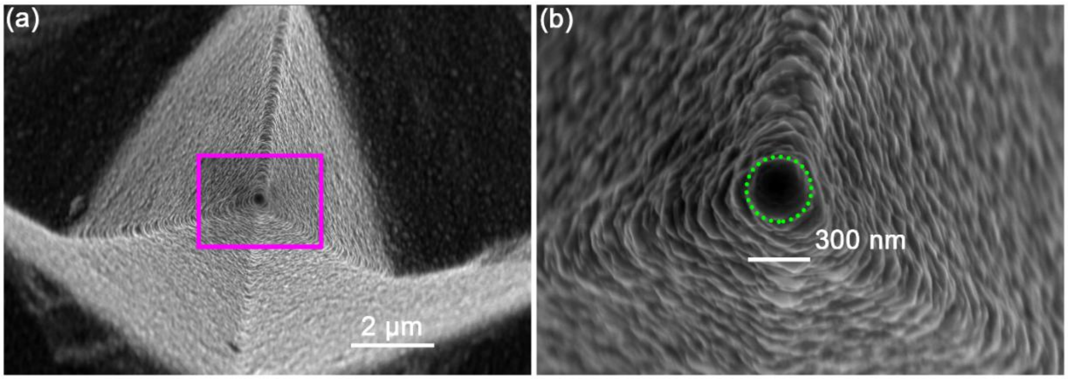

Figure S10 Characterization of AFM tip. (a) Scanning electron micrograph (SEM) images of AFM probe tip. (b) A magnified SEM image of the magenta rectangle in (a).

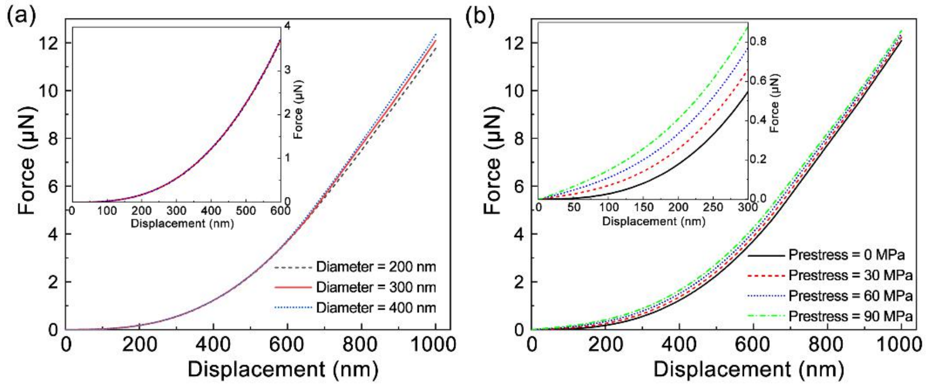

Figure S11 Error analysis of the 21.7 nm thick Au beam under nanoindentation based on FEM. (a) Effects of tip diameter on the *F*-*δ* curves. (b) Effects of prestress on the *F*-*δ* curves.

Supplemental References

[1] Rui, Z.; Rebecca, C. Mechanical Properties and Applications of Two-Dimensional Materials. In *Two-dimensional Materials*. N. Pramoda Kumar, Ed.; IntechOpen; Rijeka, 2016; pp Ch. 10.

[2] Li, P.; You, Z.; Haugstad, G.; Cui, T. Graphene fixed-end beam arrays based on mechanical exfoliation. *Appl. Phys. Lett.* **2011**, *98*, 253105.

[3] Plimpton, S. Fast Parallel Algorithms for Short-Range Molecular Dynamics. *J. Comput. Phys.* **1995**, *117*, 1-19.

[4] Hirel, P. Atomsk: A tool for manipulating and converting atomic data files. *Comput. Phys. Commun.* **2015**, *197*, 212-219.

[5] Stukowski, A. Visualization and analysis of atomistic simulation data with OVITO–the Open Visualization Tool. *Modelling Simul. Mater. Sci. Eng.* **2010**, *18*, 015012.

[6] Stukowski, A. Structure identification methods for atomistic simulations of crystalline materials. *Modelling Simul. Mater. Sci. Eng.* **2012**, *20*, 045021.

[7] Foiles, S. M.; Baskes, M. I.; Daw, M. S. Embedded-atom-method functions for the fcc metals Cu, Ag, Au, Ni, Pd, Pt, and their alloys. *Phys. Rev. B* **1986**, *33*, 7983-7991.

[8] Hill, R. The Elastic Behaviour of a Crystalline Aggregate. *Proc. Phys. Soc. A* **1952**, *65*, 349.

[9] Voigt, W. *Lehrbuch der Kristallphysik*, 1966.

[10] Reuss, A. Computation of the yield point of mixed crystals due to hiring for single crystals. *Math. Phys* **1929**, *9*, 49-58.

[11] Tersoff, J. Empirical Interatomic Potential for Carbon, with Applications to Amorphous Carbon. *Phys. Rev. Lett.* **1988**, *61*, 2879-2882.

[12] Chocyk, D.; Zientarski, T. Molecular dynamics simulation of Ni thin films on Cu and Au under nanoindentation. *Vacuum* **2018**, *147*, 24-30.

[13] Nosé, S. A unified formulation of the constant temperature molecular dynamics methods. *J. Chem. Phys.* **1984**, *81*, 511-519.

[14] Hoover, W. G. Canonical dynamics: Equilibrium phase-space distributions. *Phys. Rev. A* **1985**, *31*, 1695-1697.